

Size effects under homogeneous deformation of single crystals: A discrete dislocation analysis[☆]

P.J. Guruprasad, A.A. Benzerga^{*}

Department of Aerospace Engineering, Texas A&M University, College Station, TX 77843-3141, USA

Received 26 October 2006; received in revised form 14 March 2007; accepted 18 March 2007

Abstract

Mechanism-based discrete dislocation plasticity is used to investigate the effect of size on micron scale crystal plasticity under conditions of macroscopically homogeneous deformation. Long-range interactions among dislocations are naturally incorporated through elasticity. Constitutive rules are used which account for key short-range dislocation interactions. These include junction formation and dynamic source and obstacle creation. Two-dimensional calculations are carried out which can handle high dislocation densities and large strains up to 0.1. The focus is laid on the effect of dimensional constraints on plastic flow and hardening processes. Specimen dimensions ranging from hundreds of nanometers to tens of microns are considered. Our findings show a strong size-dependence of flow strength and work-hardening rate at the micron scale. Taylor-like hardening is shown to be insufficient as a rationale for the flow stress scaling with specimen dimensions. The predicted size effect is associated with the emergence, at sufficient resolution, of a signed dislocation density. Heuristic correlations between macroscopic flow stress and macroscopic measures of dislocation density are sought. Most accurate among those is a correlation based on two state variables: the total dislocation density and an effective, scale-dependent measure of signed density.

© 2007 Elsevier Ltd. All rights reserved.

Keywords: Dislocations; Crystal plasticity; Size effects; Finite elements; Dislocation dynamics

1. Introduction

Plastic deformation in small volumes is characterized by well documented deviations from bulk behavior. Of particular significance among these deviations is the size-dependence of plastic flow properties at the micron and sub-micron scale; see e.g. Fleck et al. (1994), Stölken and Evans (1998), Nix and Gao (1998), Swadener et al. (2002), Uchic et al. (2004), Greer et al. (2005) and Dimiduk et al. (2005). This scale dependence of strength poses serious challenges to the effective design of small-scale structures, let alone the challenge of quantifying the uncertainty that results from the spread in the values of strength upon scale reduction.

Under circumstances where a strain gradient is imposed, such as under indentation (Nix and Gao, 1998; Swadener et al., 2002), the size effect is commonly attributed to a density of geometrically necessary

[☆]This article is dedicated to Prof. Alan Needleman and Prof. Viggo Tvergaard.

^{*}Corresponding author. Tel.: +1 979 845 1602; fax: +1 979 845 6051.

E-mail address: benzerga@aero.tamu.edu (A.A. Benzerga).

dislocations (GNDs), which is needed to accommodate the so-imposed strain gradient. The connection between GNDs and what may be viewed as the plastic portion of the strain gradient is the underlying concept behind various augmented plasticity theories developed in recent years (Fleck et al., 1994; Gao et al., 1999; Fleck and Hutchinson, 2001; Acharya, 2001, 2004; Gurtin, 2002); see Forest and Sievert (2003) for an exhaustive description of several classes of non-local theories.

By way of contrast, in the absence of strain gradients existing non-local plasticity theories would predict a size-independent response. Recent experiments have yet shown compelling evidence of size-dependency in micropillar compression (Uchic et al., 2004; Greer et al., 2005; Dimiduk et al., 2005; Volkert and Lilleodden, 2006; Greer and Nix, 2006). The fact that size effects also emerge under states of macroscopically homogeneous deformation has motivated alternative explanations of size-dependent plastic behavior. Dimiduk et al. (2005) investigated possible intrinsic changes to dislocation mechanisms upon scale reduction and conclude that the observed size-dependent flow may be dominated by stochastic effects, including dislocation generation by a stress-dependent source distribution. This rationale of size-dependent flow being controlled by multiplication processes is corroborated by a number of discrete dislocation dynamics calculations of thin films (von Blanckenhagen et al., 2001), micropillar compression (Benzerga and Shaver, 2006) and grain-boundary sources (Espinosa et al., 2006). It remains that, while multiplication-controlled plasticity would significantly affect the elastic-plastic transition, it alone could not explain the effect of size on work-hardening; (e.g. Volkert and Lilleodden, 2006). It is difficult indeed to conclude from the micropillar experiments of Greer et al. (2005) and Dimiduk et al. (2005) whether the strengthening that occurs upon scale reduction is the result of increased yield strength or increased work-hardening rate at small strains.

Here we perform calculations where size effects emerge in the absence of macroscopic strain gradients and where the behavior is not multiplication controlled. Similar calculations were recently reported by Deshpande et al. (2005) but their calculations did not include forest hardening. Attention is focused on circumstances under which apparent macroscopic yield is essentially size-independent but, due to microstructure evolution, the subsequent work-hardening behavior is strongly size-dependent. In that sense, the calculations here are complementary of those of Benzerga and Shaver (2006) and Deshpande et al. (2005) and aim at providing an alternative explanation of size-dependent plastic flow at the micron scale and below.

The analyses are carried out within the framework of mechanism-based discrete dislocation plasticity (M-DDP) developed by Benzerga et al. (2004). The dislocations are modeled as line defects in a linear elastic, isotropic solid so that the long-range interactions between them are directly accounted for. Superposition is used to represent the solution of the boundary value problem of interest in terms of the infinite medium singular fields for the discrete dislocations and image fields that enforce boundary conditions (Van der Giessen and Needleman, 1995). The short-range interactions are incorporated into the formulation through a set of constitutive rules that allow for approximate representations of key three-dimensional dislocation mechanisms in a two-dimensional (2D) framework, for the purpose of computational efficiency. These rules, which may be referred to as “2.5D” rules, account for junction formation and destruction, dynamic source creation and line tension. Within this framework, the stress–strain curve, including a two-stage response (Benzerga et al., 2004), the evolution of the dislocation structure and energy storage (Benzerga et al., 2005) are outcomes of the formulation and not constitutive assumptions.

In the present investigation, geometrically similar planar crystals are subject to nominally uniform compression at fixed applied strain rate. Global as well as local measures of flow stress and dislocation density are quantified and analyzed to develop a suitable structure–property relationship in terms of reduced state variables. The results indicate that, at the micron scale, GNDs play an important role in setting the flow stress even under states of macroscopically homogeneous deformation.

2. Problem formulation

The formulation follows that of M-DDP as described by Benzerga et al. (2004). It extends the original 2D framework (Van der Giessen and Needleman, 1995) by incorporating key three-dimensional effects as a set of constitutive rules. In this mesoscopic model, plastic flow arises due to the nucleation and motion of edge dislocations modeled as line singularities in a homogeneous and isotropic elastic medium. The challenge is to solve boundary value problems involving the collective motion and interaction of a large number of discrete

dislocations. The formulation is an incremental one where at each time increment dislocation structure, stress, strain and displacements are determined. Assuming infinitesimal displacement gradients, superposition is used to describe the current state of the body in terms of the displacement, strain and stress fields as

$$\mathbf{u} = \tilde{\mathbf{u}} + \hat{\mathbf{u}}, \quad \boldsymbol{\varepsilon} = \tilde{\boldsymbol{\varepsilon}} + \hat{\boldsymbol{\varepsilon}}, \quad \boldsymbol{\sigma} = \tilde{\boldsymbol{\sigma}} + \hat{\boldsymbol{\sigma}}. \quad (1)$$

The singular ($\tilde{}$) fields are obtained by the superposition of the fields $(\mathbf{u}^i, \boldsymbol{\varepsilon}^i, \boldsymbol{\sigma}^i)$ associated with individual dislocations,

$$\tilde{\mathbf{u}} = \sum_{i=1}^N \mathbf{u}^i, \quad \tilde{\boldsymbol{\varepsilon}} = \sum_{i=1}^N \boldsymbol{\varepsilon}^i, \quad \tilde{\boldsymbol{\sigma}} = \sum_{i=1}^N \boldsymbol{\sigma}^i, \quad (2)$$

with N the total number of dislocations in the sample. The ($\hat{}$) fields are the image fields that correct for the actual boundary conditions. The latter are specified in terms of conventional tractions and displacements applied to portions of the boundary $\partial\Omega$ of a finite domain Ω . When dislocations are kept at a core distance from all boundaries, the ($\hat{}$) fields are smooth and obey a well-posed boundary value problem, which is solved using the finite element method. The glide motion of dislocation i is then determined by the Peach–Koehler force, f^i , given by

$$f^i = \mathbf{m}^i \cdot \left(\hat{\boldsymbol{\sigma}} + \sum_{j \neq i} \boldsymbol{\sigma}^j \right) \cdot \mathbf{b}^i, \quad (3)$$

where \mathbf{m}^i is the slip plane normal and \mathbf{b}^i the Burgers vector with signed length b^i and $b = |b^i|$.

Two types of Frank–Read dislocation sources are considered. Static sources are initially present with specified density and spatial distribution. Dynamic sources are formed in the course of the deformation due to dislocation interactions. Also, two types of dislocation obstacles are modeled: (i) initial stress-free point obstacles that represent precipitates; and (ii) dynamic obstacles that represent forest dislocations. The locations of initial, static sources and obstacles are randomly generated. A static source i nucleates a dipole when the magnitude of the Peach–Koehler force exceeds a critical value, $\tau_{0n}^i b$, for a prescribed time t_{0n} . The source strengths are randomly assigned from a Gaussian distribution with average $\bar{\tau}_{0n}$. The sign of the nucleated dipole depends on the sign of the Peach–Koehler force acting on the source. A dislocation may get pinned at a static obstacle and is released when the Peach–Koehler force at the location of the obstacle attains the value $\tau_{obs} b^i$, with τ_{obs} the obstacle strength.

When dislocations gliding on intersecting planes approach each other within a critical distance d^* , a junction is formed, irrespective of the sign of the interacting dislocations. Junction formation results in dynamic dislocation source and obstacle evolution during the deformation process. A junction which cannot be unzipped, for example due to cross-slip, is termed an *anchoring point*. A breakable junction is referred to as a *dynamic obstacle*. Such an obstacle is destroyed if the Peach–Koehler force acting on either dislocation comprising the junction attains or exceeds the breaking force, $\tau_{brk}^I b$. The breaking stress for junction I is configuration dependent and is given by

$$\tau_{brk}^I = \beta_{brk} \frac{\mu b}{\varphi^I}, \quad (4)$$

where φ^I is the distance to the nearest junction in any of the two intersecting planes and β_{brk} is a scaling factor for junction strength. The dislocations forming a junction are released when the latter is destroyed and are free to glide along their respective slip planes.

At the level of refinement of a 2D model, the formation of an anchoring point can only be treated as a statistical event. The probability that a junction forms an anchoring point has the prescribed value p . Anchoring points lead to the formation of new, dynamic sources. A dislocation dipole is nucleated at source I when the value of the Peach–Koehler force at either junction forming the source exceeds the value $\tau_{nuc}^I b$ during a time t_{nuc}^I . Both values depend on the local configuration and hence evolve dynamically. The nucleation stress is given by

$$\tau_{nuc}^I = \beta_{nuc} \frac{\mu b}{\varphi^I}, \quad (5)$$

where β_{nuc} is a factor that reflects source strength and \mathcal{S}^I is the distance to the nearest junction on the slip plane where τ_{nuc}^I is being resolved. The nucleation time t_{nuc}^I is given by

$$t_{\text{nuc}}^I = \gamma \frac{\mathcal{S}^I}{|\tau^I|b}, \quad (6)$$

where γ is a material constant with units of a drag factor, and τ^I is the current resolved shear stress at the location of anchoring point I , exclusive of the junction self-stress. The nucleation conditions (5)–(6) result from a dislocation multiplication model first developed by Benzerga et al. (2004) and later improved by Benzerga (2007). Their model describes the dynamic bow-out of a dislocation segment using line tension approximations.

For determining the dislocation evolution it is necessary to account for the interaction of moving dislocations with junctions. Several options are physically possible which are discussed by Benzerga et al. (2004). Here the only mechanism for junction destruction is unzipping, as described through Eq. (4). In particular, the mechanism of destruction by annihilation is not used. Thus, anchoring points cannot be broken in the simulations discussed below. Annihilation of two co-planar dislocations of opposite sign occurs by eliminating both dislocations when they are within a material-dependent critical annihilation distance, L_e , provided that none of them is involved in a junction. Dislocations are allowed to glide out of the crystal but geometry changes, such as step formation, are not accounted for.

There is an energy cost associated with the expansion of dislocation loops. But this is not explicitly taken into account in the 2D formulation with loop expansion represented by dipole separation. Hence, to represent the additional energy cost associated with loop expansion in two-dimensions, a configurational force of magnitude $\mathcal{L}^i b^i$ and pointing from one dislocation constituting the dipole toward the other is introduced with

$$\mathcal{L}^i = -\alpha \frac{\mu b}{\mathcal{S}_d^i}, \quad (7)$$

where α is the line tension parameter and \mathcal{S}_d^i the algebraic distance between the dislocations, members of the same dipole, so that the sign of \mathcal{L}^i depends on the sign of \mathcal{S}_d^i . Further details are given by Benzerga et al. (2005).

Dislocation glide is taken to be drag controlled following

$$Bv^i = \text{sign}(\tau^i + \mathcal{L}^i) \langle |\tau^i + \mathcal{L}^i| - \tau_p \rangle b^i \quad (8)$$

with B the drag factor, v^i the glide velocity of dislocation i , $\tau^i = f^i/b^i$, \mathcal{L}^i the line tension given by (7) and τ_p the Peierls stress. Note that τ^i differs from the resolved shear stress in that the stress field of dislocation i is excluded. The symbol $\langle \cdot \rangle$ denotes McCauley's brackets. To the neglect of line tension and frictional stress the right-hand side of (8) reduces to the glide Peach–Koehler force f^i defined by (3).

The difference between the M-DDP framework and other 2D discrete dislocation modeling resides in the set of additional constitutive rules (4)–(7) with (8) amended as appropriate. Accounting for these 2.5D rules is key to predicting the multi-stage hardening response of single crystals, as shown by Benzerga et al. (2004). The additional rules were derived using dislocation theory so that good estimates of all but one parameter (p which sets the probability of forming new sources) are generally known. Ranges for the parameters d^* , β_{brk} , β_{nuc} , γ and α were discussed by Benzerga et al. (2004).

Here, calculations are carried out for planar model face centered cubic crystals having dimensions $L \times H$, subject to plane strain uniaxial compression in the x_1 – x_2 plane (Fig. 1). The surfaces at $x_2 = \pm H/2$ are traction free and the shear stress vanishes at $x_1 = \pm L/2$. A uniform displacement $u_1 = \pm U/2$ is prescribed along $x_1 = \pm L/2$. The rotation of the tensile axis is not restricted. There are two slip systems oriented at $\pm\varphi_0$ from the loading x_1 -axis. The average compressive stress and the applied strain are given by, respectively,

$$\sigma = -\frac{1}{H} \int_{-H/2}^{H/2} \sigma_{11}(\pm L/2, x_2) dx_2, \quad \varepsilon = -\frac{U}{L}. \quad (9)$$

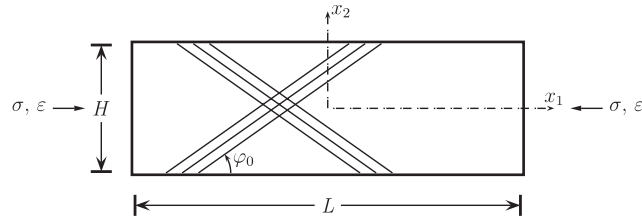


Fig. 1. Geometry of the compression problem for a planar model fcc crystal with two slip systems oriented at $\pm\varphi_0$ from the x_1 -axis.

3. Results

The calculations are carried out for geometrically similar specimens such that the aspect ratio $L/H = 3$ is kept fixed with L varied between 0.6 and 38.4 μm . The crystal orientation is defined by $\varphi_0 = 35.25^\circ$. The material parameters, $\nu = 0.3$, $\mu = 26 \text{ GPa}$, $b = 0.25 \text{ nm}$, $B = 10^{-4} \text{ Pa s}$ and $\tau_p = 0$, are taken to be representative of aluminum. The values of the parameters entering the “2.5D” constitutive rules are $d^* = 6b$, $p = 0.05$, $\beta_{\text{brk}} = \beta_{\text{nuc}} = 1$, $\gamma = 0.1B$ and $\alpha = 0$. The annihilation distance is taken to be equal to the critical distance for junction formation $L_e = d^* = 1.5 \text{ nm}$.

The analyses are carried out for initially dislocation free crystals but with potential static sources and obstacles randomly distributed on predefined slip planes, with densities $\rho_0 = 1.5 \times 10^{14} \text{ m}^{-2}$ and $\rho_{\text{obs}} = 6 \times 10^{14} \text{ m}^{-2}$, respectively. Thus, the initial source density is two orders of magnitude larger than in the microcrystals tested by Dimiduk et al. (2005). This high value of ρ_0 is chosen to promote athermal hardening processes, which were found to be ineffective at low source density (e.g. a value of 10^{12} m^{-2} was used by Benzerga and Shaver, 2006). On the other hand, the value of ρ_{obs} has little effect on the results. The mean and standard deviation of the initial source strength distribution are $\bar{\tau}_{0n} = 50$ and 10 MPa, respectively, $t_{0n} = 10 \text{ ns}$ and $\tau_{\text{obs}} = 150 \text{ MPa}$. The slip plane spacing is set to $20b$. The imposed strain rate $\dot{\epsilon} = -\dot{U}/L = 6.66 \times 10^4 \text{ s}^{-1}$ is kept the same for all specimens. A time step of $\Delta t = 0.5 \text{ ns}$ is used to resolve the dynamics of dislocation nucleation and motion. Since the results are not sensitive to mesh density when the gradients of the (\wedge) fields are resolved, a uniform finite element mesh (60 and 20 elements along x_1 and x_2 , respectively) is used for all specimens.

3.1. Flow stress and work-hardening

Typical stress versus strain responses are shown in Fig. 2 for selected specimens showing the overall transition from elastic to plastic regimes and from stage I to stage II hardening. Although the specimens are oriented for double slip from the outset, all responses exhibit some extent of stage I hardening because slip activity initiates on a few slip planes. At the scales considered here, this results in easy glide up to a few percent of strain. All specimens were taken well into stage II and some up to a strain of 0.1. The calculations corresponding to the $H = 6.4$ and 12.8 μm specimens were terminated prior to reaching the strain of 0.1 (Fig. 2b) when the number of dislocations was such that the computations were severely slowed down, e.g. over 465,000 dislocations were involved in the simulations in the $H = 12.8 \mu\text{m}$ specimen at $\epsilon \approx 0.06$.

Unlike in previous calculations (Benzerga and Shaver, 2006; Benzerga, 2007) there is no initial dislocation structure in the present calculations. Therefore, dislocation activity takes place at $\sigma \approx 105 \text{ MPa}$, irrespective of specimen size. This value is consistent with a mean source strength value of 50 MPa and a Schmid factor $f_S = (\sin 2\varphi_0)/2 = 0.47$ for both slip systems. Subsequently, there is a noticeable stress drop because the stress required for sustained plastic flow is smaller than the stress at initial yield. As shown by Benzerga and Shaver (2006) and Benzerga (2007), the post-yield stress drop can be eliminated by incorporating an initial dislocation structure.

The specimen size affects the stress–strain curve in a number of respects. To quantify the size effect, the values of the 0.2% yield strength, σ_y , the rate of stage I hardening, Θ_I , the stress at the beginning of stage II,

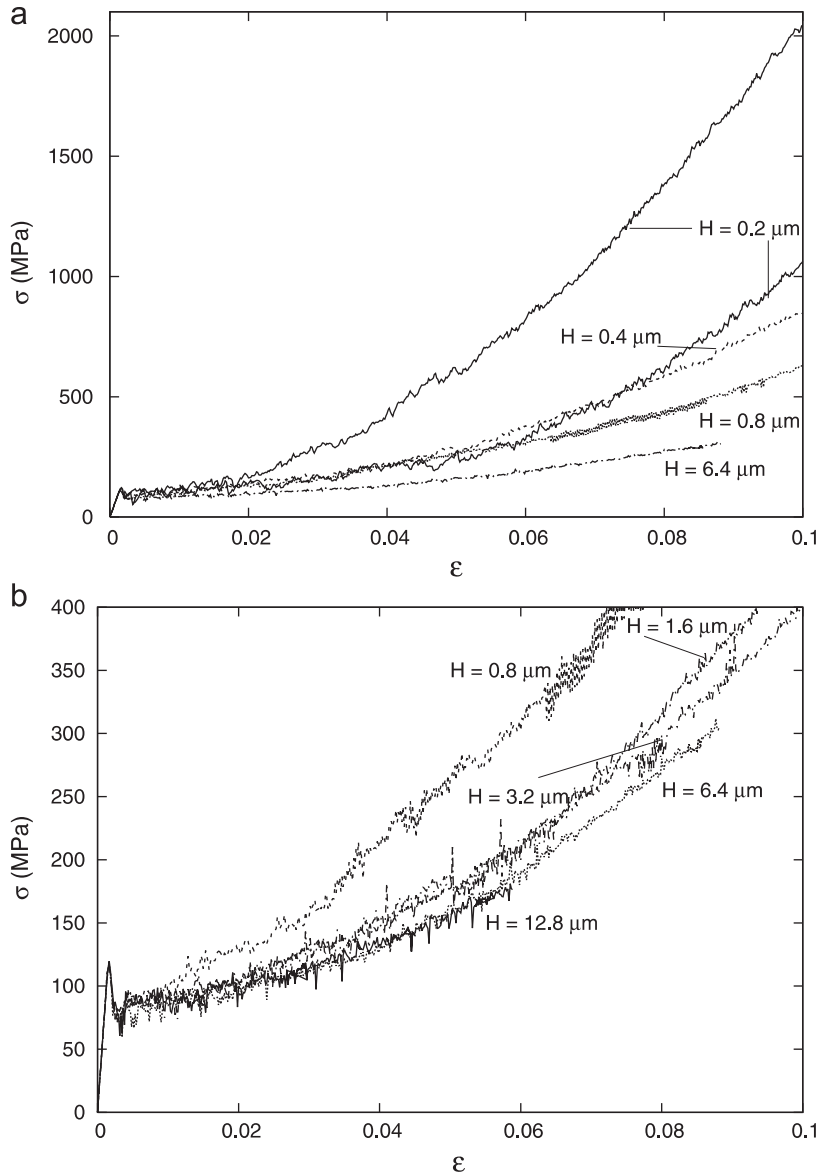


Fig. 2. Representative stress versus strain compression responses of the (a) $H = 0.2, 0.4, 0.8$ and $6.4 \mu\text{m}$ specimens; and (b) $H = 0.8, 1.6, 3.2, 6.4$ and $12.8 \mu\text{m}$ specimens. A reduced stress range is shown in (b) and two realizations of the $H = 0.2 \mu\text{m}$ specimen are shown in (a).

σ_{II} , and the rate of stage II hardening, Θ_{II} , are reported in Table 1. For most specimen sizes three values are given which correspond to distinct realizations of the initial static source and obstacle distributions. The precise definition of the parameters listed in the table is given in Fig. 3. The instantaneous work-hardening rate is defined as $\Theta = d\mathcal{T}/d\Gamma$, where $\mathcal{T} = f_S\sigma$ and $\Gamma = \varepsilon/f_S$, respectively, refer to the macroscopic flow stress and shear strain, resolved on either slip system.

Most notable in the stress–strain curves of Fig. 2 is the effect of size on the stage II hardening rate, Θ_{II} . As shown in Table 1 other characteristics of the stress–strain response are also size-dependent. While the values of the yield strength σ_y exhibit a slight increase with decreasing specimen size (roughly 20% over the size range investigated) those of σ_{II} increase by nearly a factor of 3. Correspondingly, the stage I hardening rate, Θ_I , increases by one order of magnitude, Table 1. The increase in the spread of the values of all characteristics with decreasing specimen size is also noteworthy.

Table 1
Characteristics of the multi-stage hardening response of geometrically similar crystals with a length to height ratio of 3

Size, H (μm)	σ_y (MPa)	σ_{II} (MPa)	Θ_I/μ	Θ_{II}/μ
0.2	80	258.3	0.0366	0.192
	115	175.0	0.0114	0.244
	77	208.3	0.0175	0.239
0.4	95	186.6	0.0132	0.119
	95	213.3	0.0179	0.128
	75	211.1	0.0172	0.080
0.8	75	200.0	0.0193	0.071
	90	190.0	0.0186	0.065
	85	151.1	0.0114	0.065
1.6	80	156.0	0.0117	0.055
	75	152.0	0.0125	0.044
	80	160.0	0.0131	0.050
3.2	80	107.5	0.0053	0.037
	65	100.0	0.0049	0.032
	72	133.3	0.0099	0.039
6.4	70	101.7	0.0047	0.024
	75	101.9	0.0041	0.029
12.8	90	93.5	0.0030	0.022
	75	90.9	0.0026	0.018

The symbols σ_y , σ_{II} , Θ_I and Θ_{II} refer to the 0.2% yield strength, the flow stress at the beginning of stage II, the rate of stage I hardening and the rate of stage II hardening, respectively. Up to three realizations are reported for each specimen size.

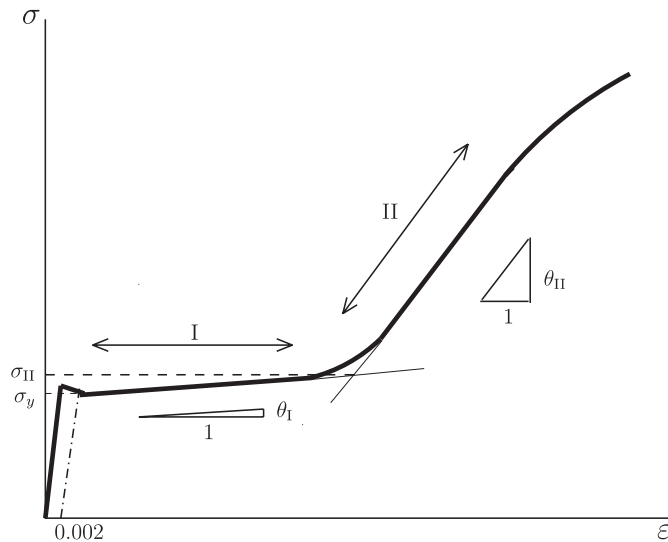


Fig. 3. Sketch of a typical stress–strain multi-stage response of a single crystal showing the definition of the strength and hardening quantities listed in Table 1. Here $\theta_i = \Theta_i/f_S^2$ ($i = \text{I, II}$).

Fig. 4a depicts the values of the flow stress, σ_f , as a function of specimen height, H , at various strain levels. Because of strain hardening the scaling of σ_f with size varies in the course of deformation. A power law of the form

$$\frac{\sigma_f}{\sigma_0} \equiv \frac{\mathcal{F}}{f_S \sigma_0} = \left(\frac{H}{H_0} \right)^{-x} \quad (10)$$

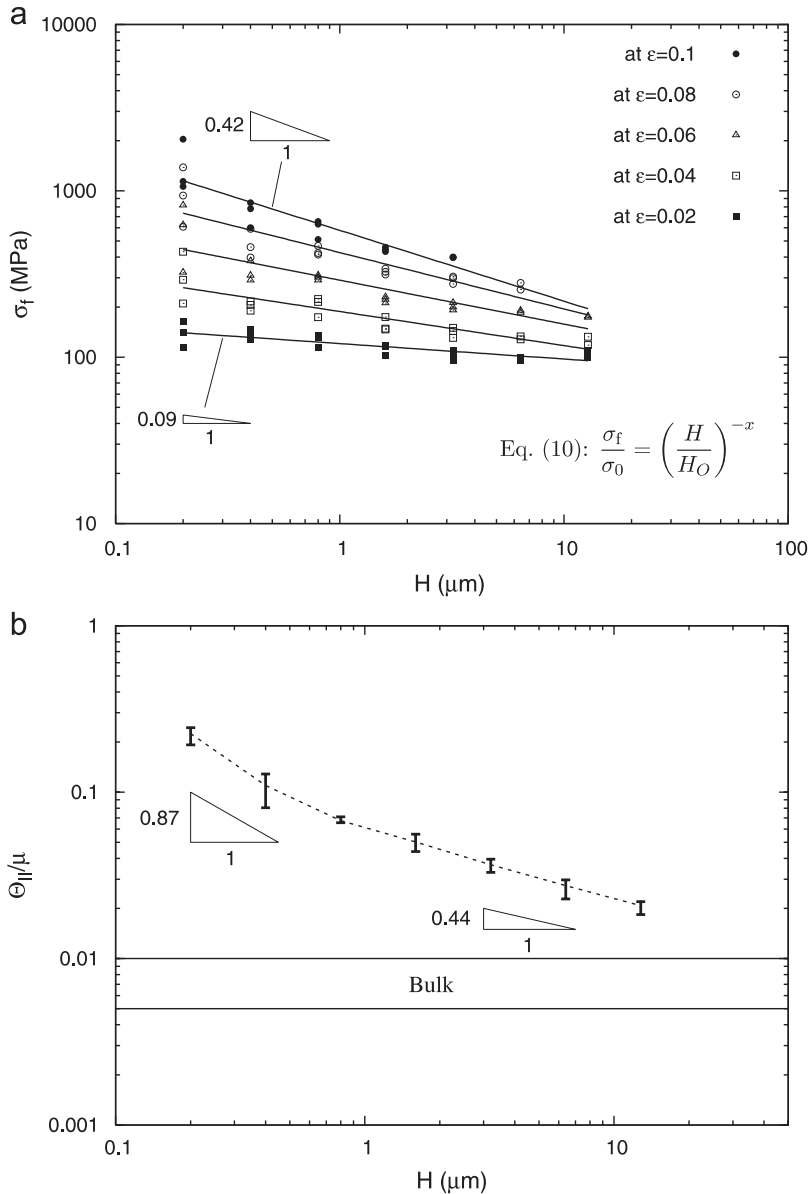


Fig. 4. (a) Flow stress, σ_f , versus crystal height, H , at various strain levels. Best fit lines following power law (10) are based on two or three realizations per specimen size. The value of the scaling exponent x in (10) is 0.09, 0.2, 0.26, 0.33 and 0.42 at $\epsilon = 0.02, 0.04, 0.06, 0.08$ and 0.1, respectively. (b) Stage II work hardening rate, Θ_{II} , in units of the shear modulus μ , versus crystal height, H , showing two distinct scaling regimes with the best power law fits exhibited. Bounds of scatter bars correspond to actual maxima and minima from several realizations and averages are connected by the dotted line. Horizontal lines depict the typical, material-independent range of bulk values of Θ_{II}/μ .

fits relatively well the data in Fig. 4a at all strain levels but the scaling exponent x increases from ≈ 0.1 at $\epsilon = 0.02$ to over 0.4 at $\epsilon = 0.1$.

The effect of specimen size on stage II hardening is quantified in Fig. 4b. The work-hardening rate Θ_{II} increases steadily with decreasing specimen size. The $\mu/200$ to $\mu/100$ range of bulk values of Θ_{II} is also depicted in Fig. 4b for comparison purposes. In the $H = 0.2 \mu\text{m}$ specimen, the calculated value of Θ_{II} , averaged over three realizations, is about 20 times larger than the maximum bulk value. By way of contrast, in the largest specimen analyzed, the value of Θ_{II} is less than twice the bulk value. In addition, it is worth noting that the effect of size on Θ_{II} is enhanced for values of H in the sub-micron regime.

3.2. Evolution of the dislocation structure

Fig. 5 shows the dislocation density, ρ , versus strain curves corresponding to the overall stress–strain responses in Fig. 2. Up to a strain of about 0.04 the evolution of the dislocation density is insensitive to specimen size. Beyond the 0.04 strain level the rate of increase of ρ is consistently increased with decreasing specimen size. In addition, for fixed specimen dimensions, the rate of dislocation accumulation decreases with increasing strain for $\varepsilon < 0.04$ so that the curves are concave downward. By way of contrast, the increase in ρ for $\varepsilon > 0.04$ is rather linear, except for the largest two specimens where the density versus strain curves retain the slightly concave shape.

The corresponding evolution of total junction density is shown in Fig. 6a. The junction density increases with strain for specimens of all sizes, but there is a noticeable decrease in the junction production rate after some straining. Similar trends are obtained for the dynamic obstacle density (Fig. 6b) but the production rate of obstacles vanishes with continued deformation. This is due to the fact that after sufficient strain hardening, stress levels are so high that obstacles are more easily broken. Although not shown in the figure, the results indicate that the dynamic source production also decreases in rate with increasing strain but does not saturate. Anchoring points cannot be destroyed but large back-stresses on densely packed slip planes tend to shut down the sources located on these planes. This ultimately leads to a decrease in the production of dynamic sources.

Beyond the details of dislocation structure evolution described above, it is emphasized that there is little correlation between junction density and specimen size, at fixed overall strain. The dynamic obstacle density shows a more consistent decrease with increasing specimen size, but only for $H > 0.8 \mu\text{m}$. Whether all junctions or only the dynamic obstacles are chosen to represent the forest, the size-dependence of the flow stress cannot be correlated with the spacing between forest dislocations.

The dislocation distributions corresponding to a strain of 0.1 are shown in Fig. 7 for selected specimen sizes. Positive dislocations are shown in black whereas negative dislocations are shown in gray. Two specimens with $H = 0.2 \mu\text{m}$ are shown to highlight the increased variability of the results in smaller specimens. In one realization of the $H = 0.2 \mu\text{m}$ specimen, the dislocation structure (Fig. 7a, left) shows an excess of negative dislocations within the specimen, i.e. a residual Burgers vector. Interestingly, this realization is characterized with a higher flow stress and a larger value of the stage II hardening rate; see Fig. 2. In all other specimens the ratio of signed to total dislocation density at $\varepsilon = 0.1$ essentially vanishes over the volume of the specimen.

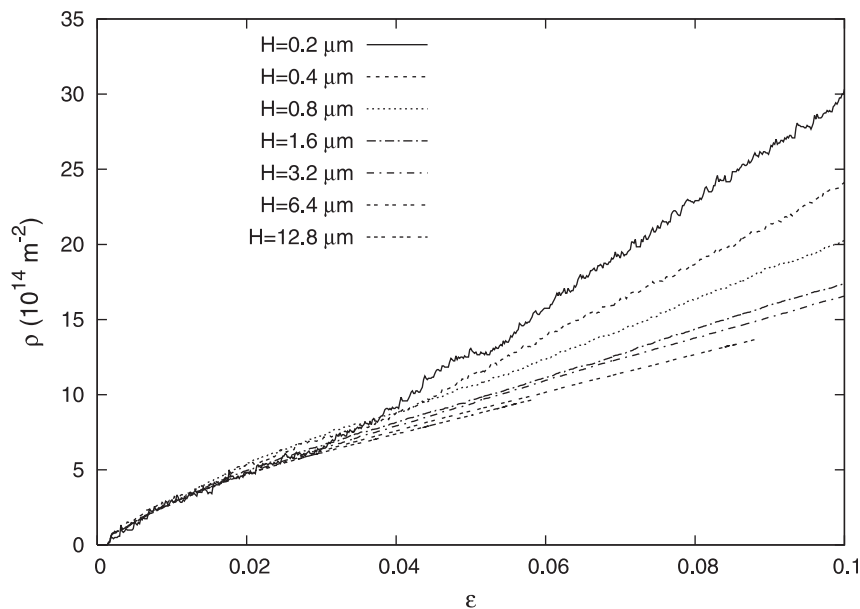


Fig. 5. Evolution of dislocation density with strain for selected realizations of all specimen sizes corresponding to the stress–strain responses of Fig. 2.

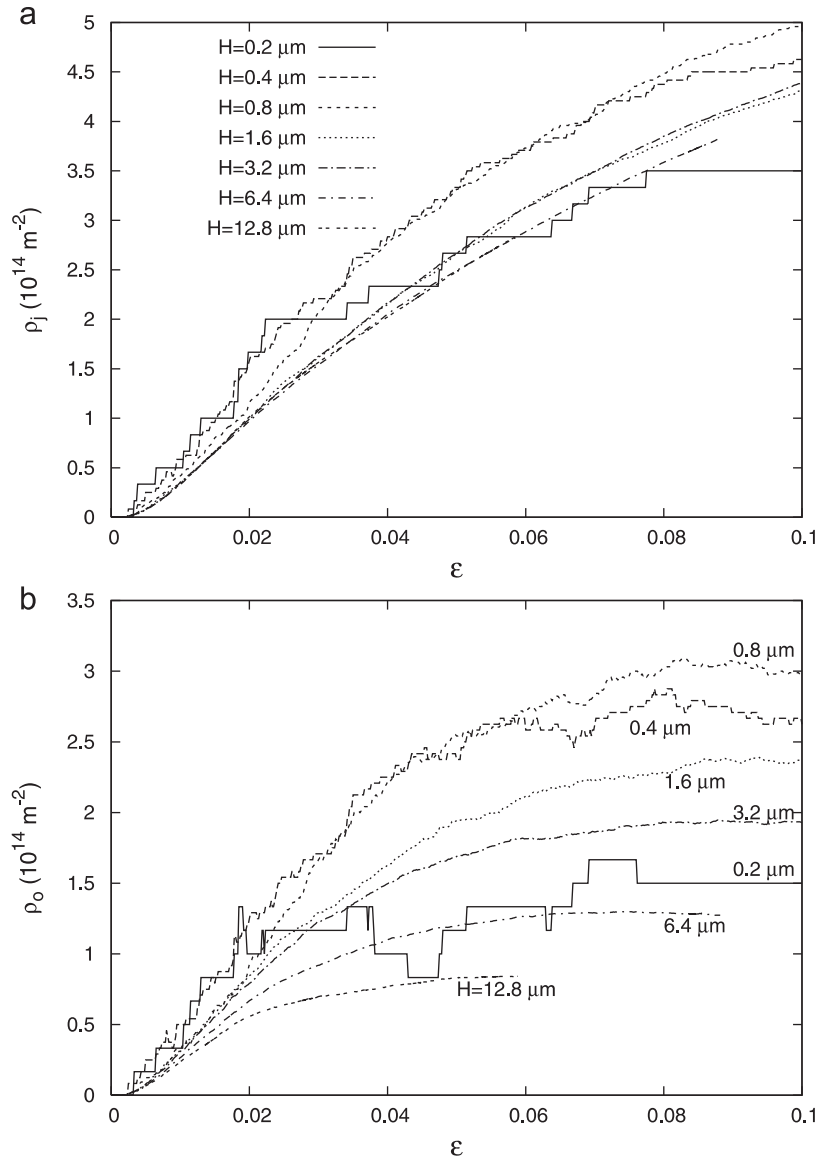


Fig. 6. (a) Total junction density versus strain for selected realizations of all specimen sizes; (b) corresponding evolution of dynamic obstacle density. At fixed strain $d\rho_o \leq d\rho_j$ since $\rho_j = \rho_o + \rho_a$ and the density ρ_a of anchoring points can only increase with strain or remain constant.

3.3. Flow stress scaling

In physical theories of crystal plasticity, the dislocation density is commonly used as the structural parameter for macroscopic descriptions of plastic flow, with the flow stress governed by Taylor-like hardening following

$$\mathcal{T} = A\mu b\sqrt{\rho}, \quad (11)$$

where A is a constant in the range 0.3–0.5 when the athermal component of \mathcal{T} is retained (Gil Sevillano, 1993). Fig. 8 shows the evolution of \mathcal{T} with strain for selected specimen sizes. The flow stress is given in units of $\mu b\sqrt{\rho}$ to explore the validity of Eq. (11) at the micron scale. This plot clearly shows that the increase in dislocation density with decreasing specimen size (Fig. 5) does not suffice to explain the corresponding

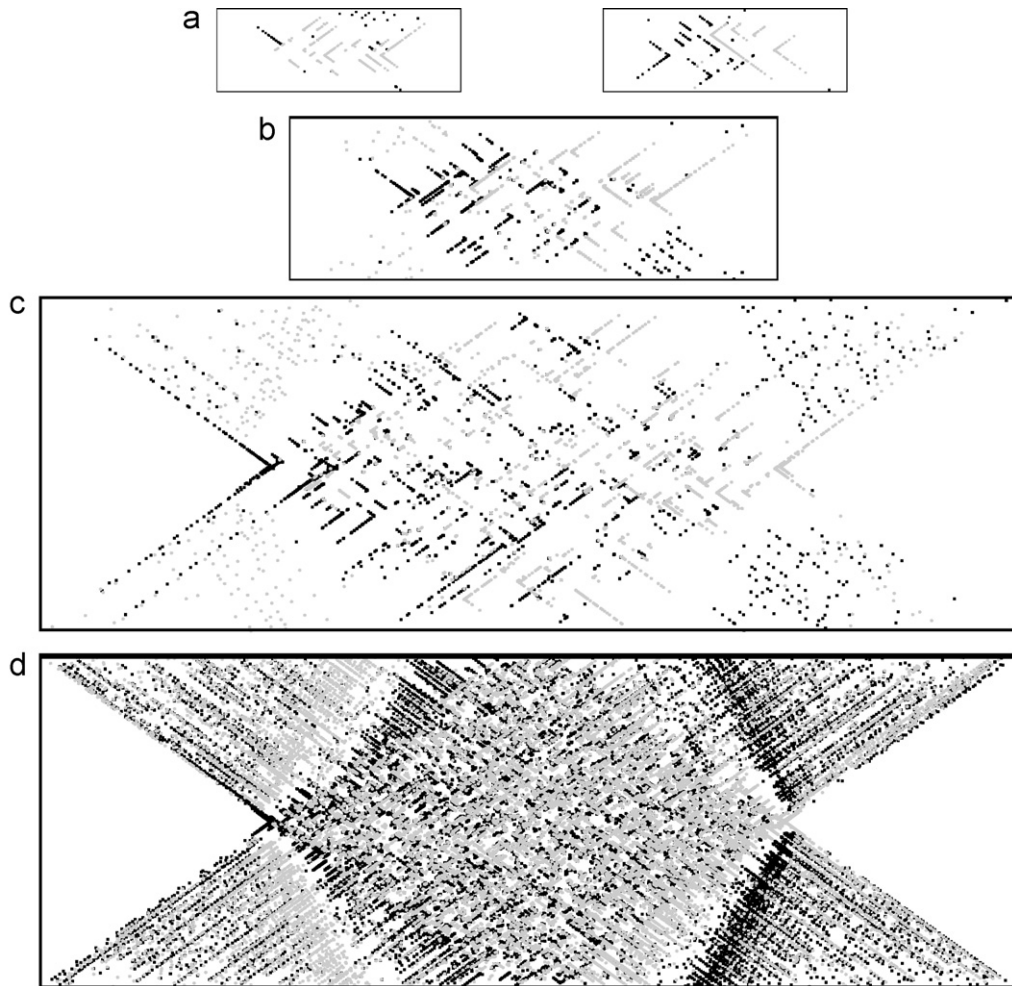


Fig. 7. Spatial distribution of dislocations at $\varepsilon = 0.1$ in the crystals of height (a) $H = 0.2 \mu\text{m}$; (b) $H = 0.4 \mu\text{m}$; (c) $H = 0.8 \mu\text{m}$ (all scaled appropriately); and (d) $H = 3.2 \mu\text{m}$ (not scaled). Positive dislocations are shown as black dots whereas negative dislocations are shown as gray dots. Two realizations are shown for the $H = 0.2 \mu\text{m}$ specimen as in Fig. 2.

increase of the flow stress (Fig. 2). At fixed specimen size, there is a deformation regime where the bulk scaling law (11) holds with values of the pre-factor A within the range 0.3–0.5. The bigger the sample the larger the extent of this regime and the smaller the value of A . But a deviation from this behavior takes place for all specimen sizes. This deviation is more pronounced in stage II and is larger in magnitude for smaller specimens. The behavior in Fig. 8 indicates that, at the micron scale: (i) the dislocation density does not suffice to set the flow stress; and (ii) the spatial distribution of dislocations affects the flow stress, in a way not specified as yet, and this effect is inherently increased with decreasing sample size.

3.4. Local flow stress and dislocation density

In principle the applied loading can be accommodated by a uniform stress distribution. However, the presence of a dislocation structure and the heterogeneity of dislocation mediated slip lead to an inhomogeneous stress distribution. Fig. 9 shows contours of the axial stress σ_{11} corresponding to selected specimen sizes at a strain $\varepsilon = 0.1$. The corresponding dislocation structures were shown in Fig. 7. In any given specimen, the spatial average of σ_{11} over the volume corresponds, in magnitude, to the overall stress given by Eq. (9). Clearly, at a strain of 0.1 the heterogeneous internal stress field has evolved in such a way that surface

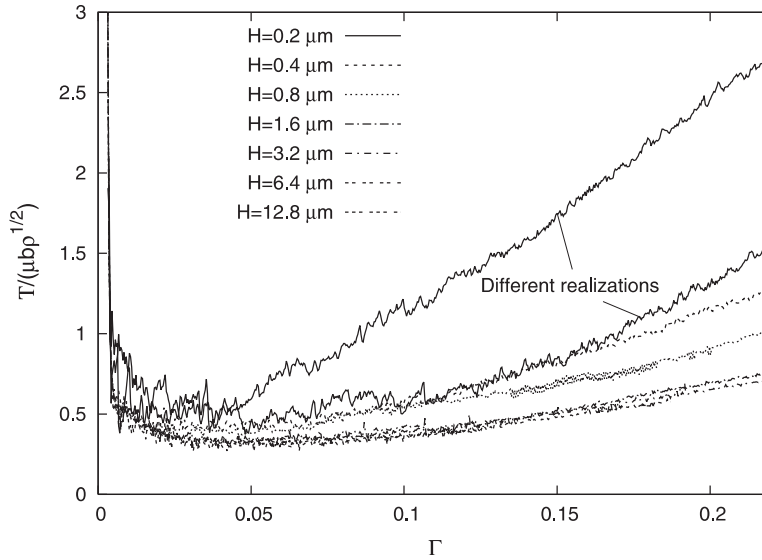


Fig. 8. Macroscopic flow stress, $\mathcal{T} = f_S \sigma$, in units of $\mu b \sqrt{\rho}$, versus macroscopic resolved shear strain, $\Gamma = \varepsilon / f_S$, with $f_S = 0.47$ the Schmid factor. The specimen realizations correspond to those in Figs. 2 and 5 for the stress–strain and density–strain curves, respectively.

boundary layers have formed which are softer than the core of the specimen. The fact that the core is harder than regions located near the free surfaces is consistent with the experimental measurements of [Fourie \(1968\)](#). In the calculations, the formation of a hard core between softer boundary layers is associated with the increased propensity of dislocation intersections within the core, which enhance junction formation and subsequent forest hardening mechanisms.

In [Fig. 9a](#) two specimens with $H = 0.2 \mu\text{m}$ are considered just like in [Fig. 7a](#). The stress distributions are quite different in the two samples, especially at the strain of 0.1. In the sample shown on the right, stress concentrates along a band and this may contribute to lower the overall flow stress and work-hardening rate. This picture, together with the build-up of a residual Burgers vector in the sample shown on the left (recall [Fig. 7a](#)) is consistent with the scatter in the Θ_{II} values shown in [Fig. 4b](#).

In order to quantify the flow stress variation across specimen height, averages of the axial stress were calculated over strips of equal thickness h , running parallel to the specimen axis. Define $\Sigma_{11}(x_2^n) = \langle \sigma_{11}(x_1, x_2) \rangle_{\Omega^n}$ with $\langle \cdot \rangle_X$ the spatial average over X and Ω^n a strip-like domain defined by $-L/2 \leq x_1 \leq L/2$ and $-h/2 \leq x_2 - x_2^n \leq h/2$ where $x_2^n = (n - \frac{1}{2})h - H/2$ refers to the center-coordinate of the strip. [Fig. 10](#) shows the so-averaged axial stress, Σ_{11} , against the x_2 location of the strip.

The stress profiles in [Fig. 10](#) reveal a number of interesting features. First, in any given specimen the flow stress is typically 3 times as large in the core than near the surface. Second, there essentially is a pointwise increase of the flow stress when the specimen size decreases. We may also notice that the flow stress is not uniform in the soft boundary layers. It attains a minimum at a distance, roughly 10–15% of the total specimen height, from the free surface. This effect is associated with the formation of nearly dislocation-free thin layers in the vicinity of the top and bottom free surfaces ([Fig. 7](#)). These thin layers are harder than regions located farther away from the surface ([Fig. 9](#)).

Also noticeable in [Fig. 10](#) is the symmetry of the stress distribution about the x_1 -axis for all but one realization of the $H = 0.2 \mu\text{m}$ specimen. The asymmetry of the latter, already noticeable at $\varepsilon = 0.033$ ([Fig. 10a](#)), is such that the flow stress in the bottom half of the specimen is larger than the average flow stress of the whole specimen, which is approximately 2 GPa; see [Fig. 2](#). This means that a tendency to bending has occurred inside the specimen, superposed onto the overall compressive stress state. This is consistent with the picture in [Fig. 7a](#) (left) and a residual Burgers vector. Although a significant portion of the strengthening in the $H = 0.2 \mu\text{m}$ specimen discussed above may be associated with a density of GNDs induced by local lattice rotations within the specimen, this behavior does not explain the size-dependence of flow stress and strain hardening depicted in [Figs. 2](#) and [4](#) for $H \geq 0.4 \mu\text{m}$. Indeed, the net Burgers vector in all specimens with

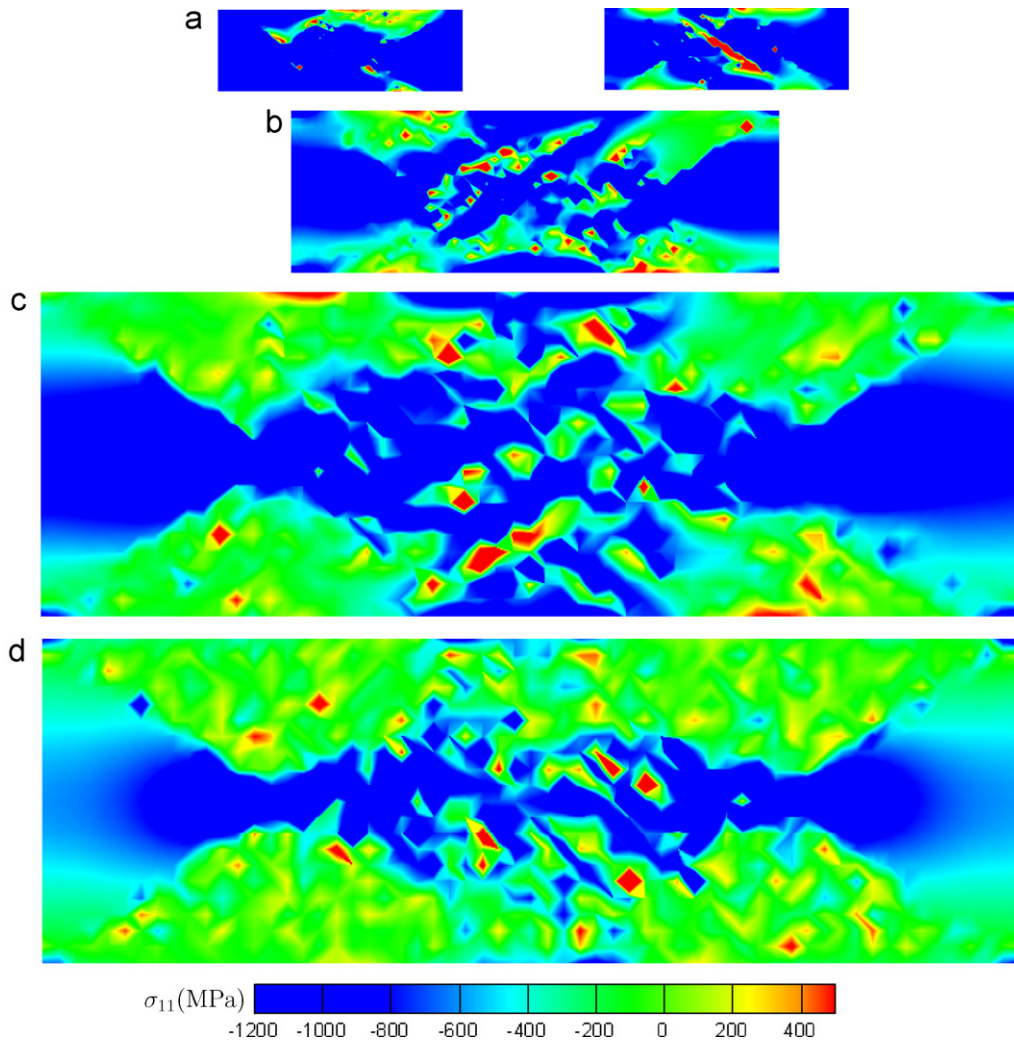


Fig. 9. Contours of axial stress σ_{11} at $\varepsilon = 0.1$ in crystals of height (a) $H = 0.2\mu\text{m}$; (b) $H = 0.4\mu\text{m}$; (c) $H = 0.8\mu\text{m}$ (all scaled appropriately); and (d) $H = 3.2\mu\text{m}$ (not scaled). Two realizations are shown for the $H = 0.2\mu\text{m}$ specimen as in Fig. 7.

$H \geq 0.4\mu\text{m}$ is negligible in magnitude. As shown in Fig. 10b, the whole stress profiles are shifted toward larger stresses when the specimen size is decreased.

While the Taylor hardening equation (11) does not hold overall, the question arises as to whether it is valid locally. Local dislocation densities were calculated, consistent with the local flow stress definition above. The height h of the domains Ω^n sets the window of resolution. The dislocation density profiles obtained at a strain $\varepsilon = 0.1$ and using a resolution $h = 40\text{nm}$ are shown in Fig. 11a for selected specimens. As expected, the distribution has a rather symmetric bell shape with the dislocation density being greater within the core region than outside of it. Fig. 11b depicts the deviation of local flow stress from what would have been its value had Taylor hardening applied locally. The deviation is minimum near the surfaces and maximum at the center. These plots clearly show that Taylor hardening breaks down at the microscopic scale as well.

3.5. Distribution of local GND density

Since the size-dependence of the overall flow stress is associated with an increase in stress throughout the specimen and not only within the core, the question addressed now is that of what relationship there is, if any, between local flow stress and local dislocation density. In particular, the way in which the signed dislocation

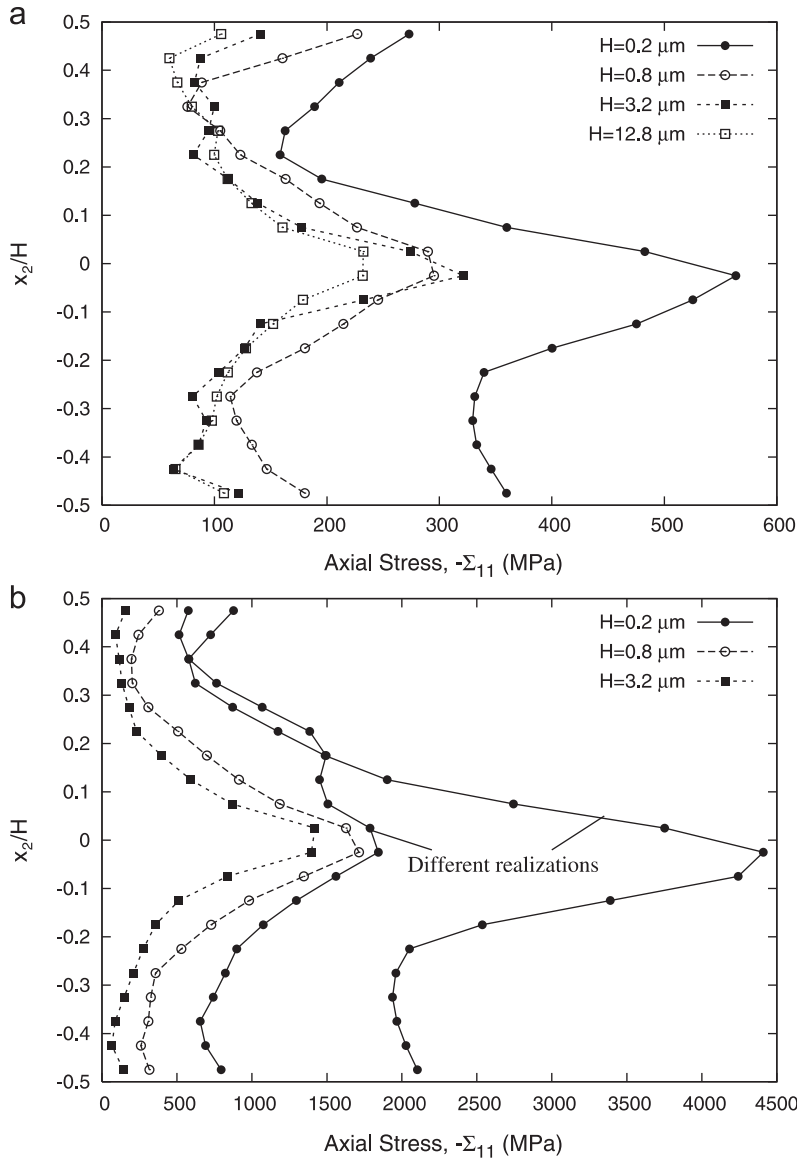


Fig. 10. Variation of the flow stress across the crystal height for selected specimen sizes: (a) at $\epsilon = 0.033$; and (b) at $\epsilon = 0.1$. The local flow stress is identified with $|\Sigma_{11}|$, the axial stress averaged over horizontal domains.

density affects the local flow stress is of interest. The densities of positive and negative dislocations on slip-system κ , $\rho_+^{(\kappa)}$ and $\rho_-^{(\kappa)}$, respectively, were evaluated separately. The signed, or GND, density for slip-system κ is defined as $|\rho_+^{(\kappa)} - \rho_-^{(\kappa)}|$. The total GND density, ρ_G , is defined using the net Burgers vector based on Nye's tensor (see Appendix A).

Clearly, both $|\rho_+^{(\kappa)} - \rho_-^{(\kappa)}|$ and ρ_G are resolution-dependent. Fig. 12a shows the through-thickness distribution of ρ_G corresponding to four different values of the resolution h in the $H = 3.2 \mu\text{m}$ specimen strained to $\epsilon = 0.1$. The method used to define local densities is the same as in the previous section. At the coarsest resolution $h = H$ the GND density only represents 0.3% of the total dislocation density, consistent with a macroscopically homogeneous deformation. However, a local GND density emerges at sufficient resolution. It peaks at the center of the specimen but all values are significant relative to the total dislocation density. As expected, the local GND density is highly resolution-dependent: the finer h the higher the fluctuations in ρ_G .

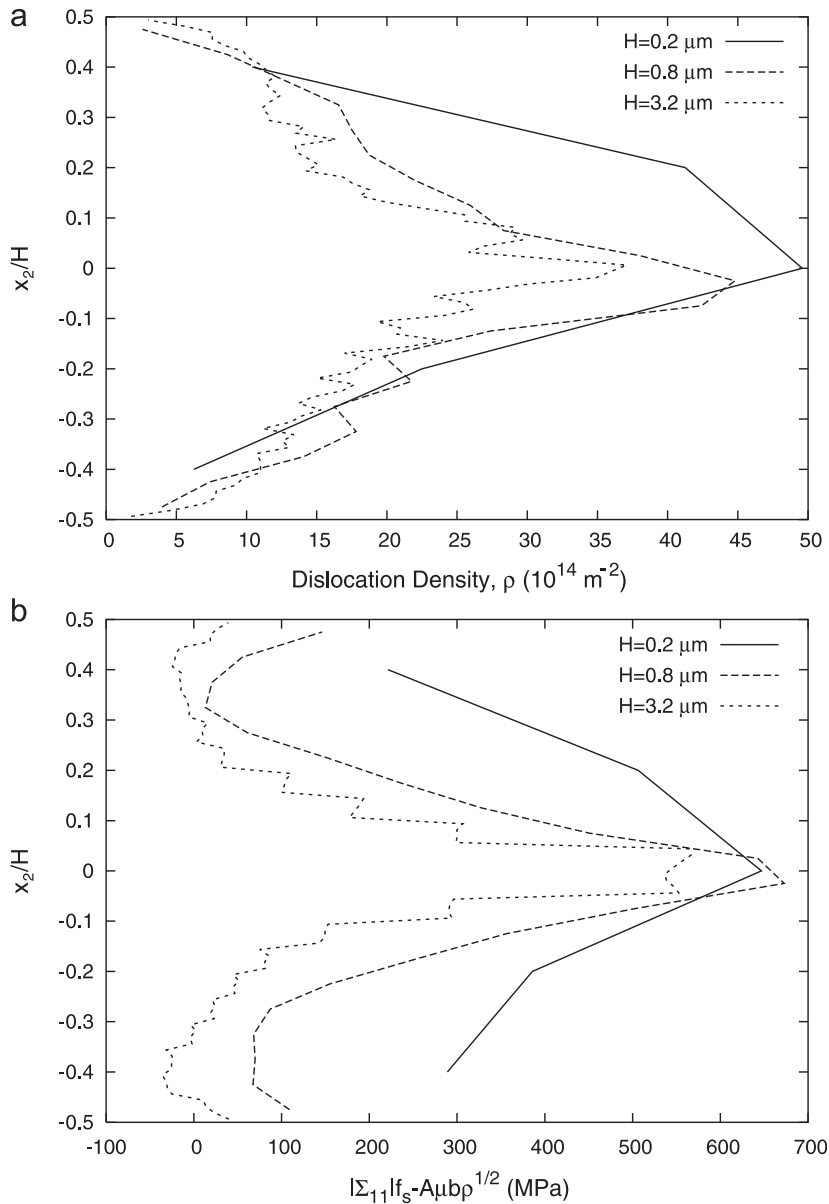


Fig. 11. (a) Variation of the dislocation density across the crystal height for selected specimen sizes at $\varepsilon = 0.1$. Local densities are calculated in horizontal domains of equal thickness $h = 40 \text{ nm}$ (see text). (b) Corresponding deviation of the local flow stress from ideal Taylor hardening, Eq. (11) with $A = 0.3$. Both Σ_{11} and ρ are evaluated at the same resolution $h = 40 \text{ nm}$.

Fig. 12b depicts the through-thickness distribution of the GND density for the three specimens shown in Fig. 11 at $\varepsilon = 0.1$, in addition to one $H = 12.8 \mu\text{m}$ specimen at $\varepsilon = 0.056$. The same resolution $h = 50 \text{ nm}$ was used for all specimens. This value of h is sufficiently small in comparison with the smallest specimen ($H = 0.2 \mu\text{m}$) but large enough so that individual domains contain on average a large number of dislocations. Typically, at $\varepsilon = 0.1$ there were about 60 and 630 dislocations per domain analyzed in the $H = 0.2$ and $3.2 \mu\text{m}$ specimens, respectively. Fig. 12b reveals a trend for increasing local GND density upon a decrease in specimen size. The same trend is obtained when each slip system is analyzed separately.

It is worth emphasizing that, in all specimens with $H \geq 0.4 \mu\text{m}$, the net GND density represents less than 10% of the total density up to $\varepsilon = 0.1$. Although the imposed deformation is macroscopically homogeneous a GND density emerges in microscopic domains. This finding highlights the role of a locally non-vanishing

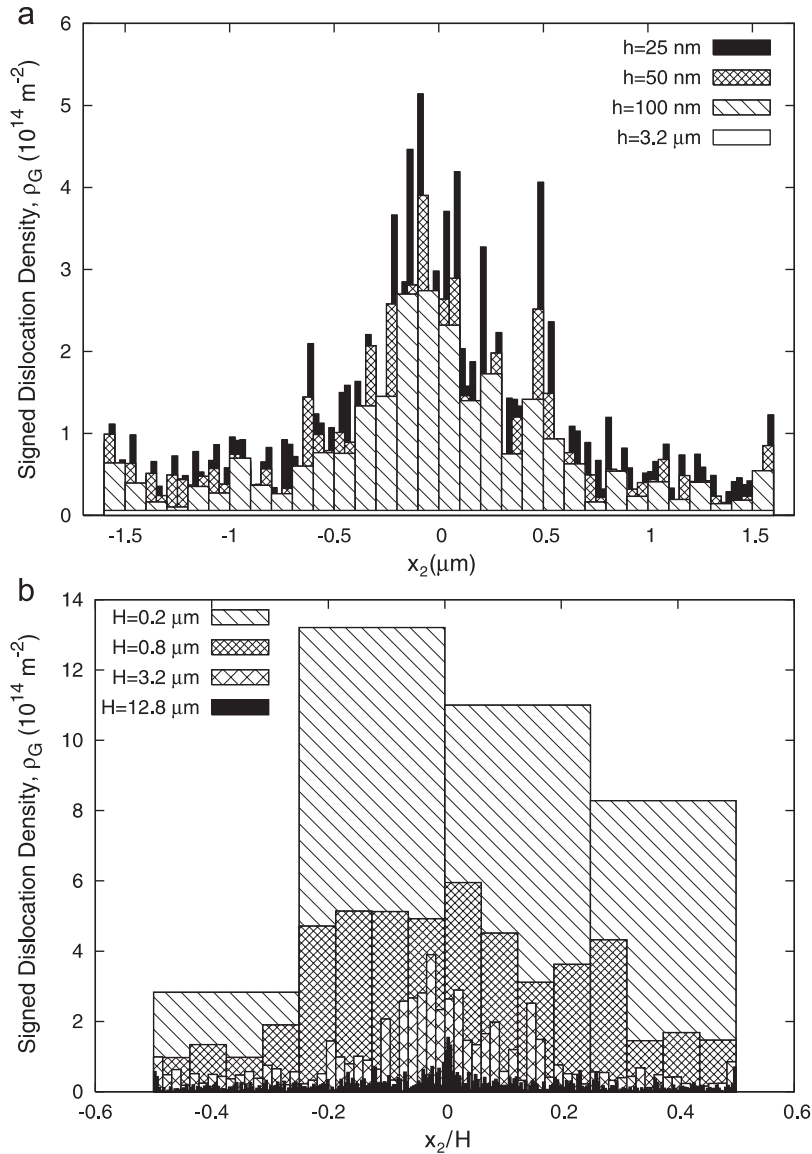


Fig. 12. Variation of the signed dislocation density, ρ_G , across crystal height at $\varepsilon = 0.1$: (a) effect of the resolution h on ρ_G in the $H = 3.2 \mu\text{m}$ specimen; (b) effect of specimen size on ρ_G evaluated at the same resolution $h = 50 \text{ nm}$ for selected specimen sizes at $\varepsilon = 0.1$. For the specimen with height $12.8 \mu\text{m}$ the ρ_G was evaluated at a strain of $\varepsilon = 0.056$. The signed or GND density ρ_G is calculated using (A.5).

GND density in setting the local, and by way of consequence, the global flow stress. Quantifying the relationship between local flow stress and local GND density is, however, not a trivial task in view of the fact that the GND density is dependent upon resolution and vanishes overall. Only macroscopic, heuristic correlations can be envisaged using appropriately defined GND measures. One such correlation is developed in Section 3.7 below.

3.6. Bauschinger effect

In view of the build-up of a signed dislocation density at the micro-scale, significant back-stresses arise which contribute to the apparent work-hardening. In an attempt to quantify the effect of such back-stresses,

all specimens were unloaded to $\sigma = 0$. Fig. 13 shows the stress versus strain curves corresponding to unloading from two strain levels. Reverse plasticity takes place in all cases prior to complete unloading. This indicates a Bauschinger effect. When unloading from $\varepsilon = 0.033$, i.e. roughly the end of stage I, the Bauschinger effect is small in all specimens with $H \geq 0.4 \mu\text{m}$ in comparison with the $H = 0.2 \mu\text{m}$ specimen (Fig. 13a). By way of contrast, unloading from $\varepsilon = 0.067$ reveals a strong Bauschinger effect in all specimens that were deformed up to that strain (Fig. 13b). The $H = 12.8 \mu\text{m}$ specimen was unloaded from the highest strain of 0.057 reached in the forward loading calculation. The corresponding curve is also shown in Fig. 13b.

In an accompanying paper we use a strain measure of the Bauschinger effect to show that the latter increases in magnitude with decreasing specimen size. Here, what we abstract from the results in Fig. 13 is that a significant portion of the simulated strain hardening is due to back-stresses associated with the rise of

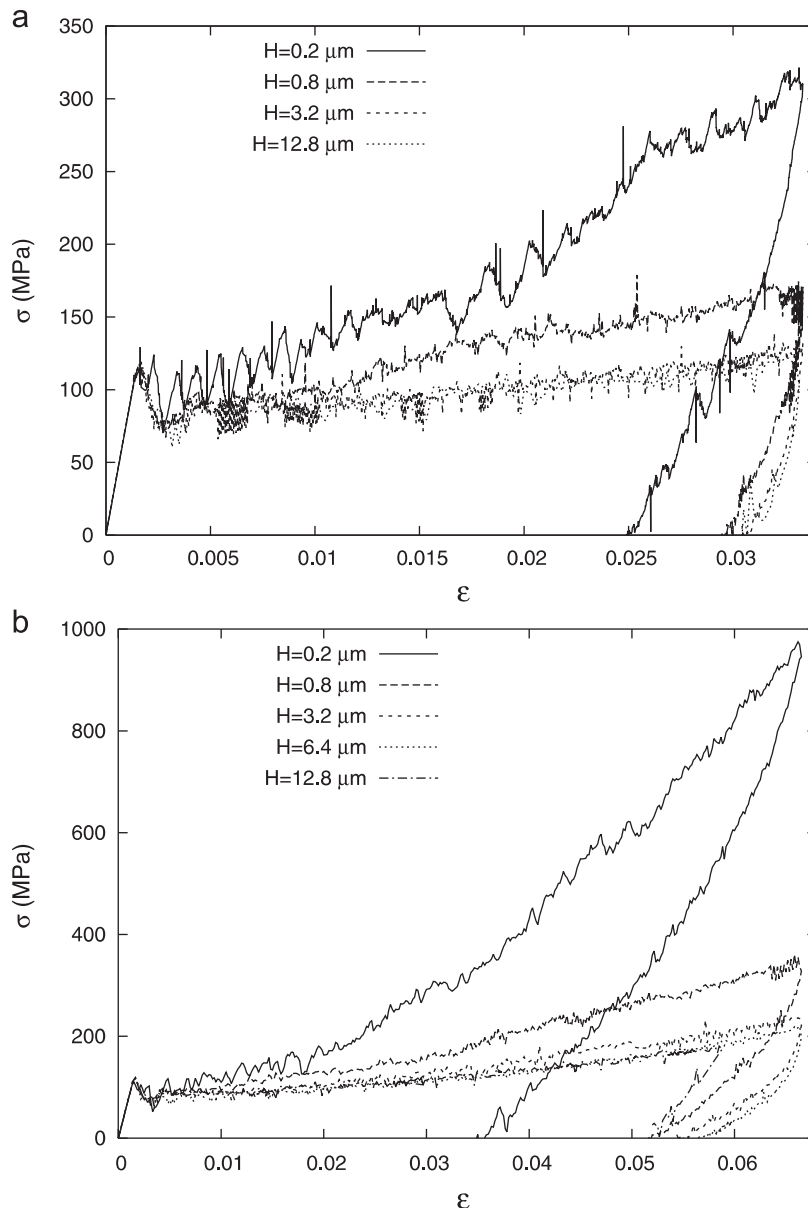


Fig. 13. Selected stress versus strain curves with unloading to $\sigma = 0$ from a strain of: (a) $\varepsilon = 0.033$ showing a small Bauschinger effect. More data points are used to plot the loading and unloading behavior; and (b) $\varepsilon = 0.067$ showing a strong Bauschinger effect.

a micro-scale GND density. While the GND density vanishes at the macro-scale, the back-stress does not, because of its long-range character.

3.7. Development of a scaling law

The key features of the discrete dislocation analyses carried out here may be summarized as follows: (i) Taylor hardening breaks down globally and locally; (ii) the microscopic GND density does not vanish as opposed to the macroscopic GND density; and (iii) a significant portion of the observed strain hardening must be associated with evolving back-stresses. With this in mind, it would be useful to develop a relationship between flow stress and appropriately chosen structural variables, it being understood that the total dislocation density alone does not describe the current state. Conclusions (ii) and (iii) above will guide the development of this new scaling law.

First, to describe the current state, the dislocation density is supplemented with an additional variable that may be viewed as an integral measure of the microscopic GND density. For each slip-system κ , define

$$\bar{\rho}_G^{(\kappa)} = \sum_{n=1}^p \frac{\Omega^n}{\Omega} |\rho_{+n}^{(\kappa)} - \rho_{-n}^{(\kappa)}|, \quad (12)$$

where the local signed density is evaluated within domains Ω^n of resolution h that make up volume Ω . Here, $\Omega^n/\Omega = h/H = 1/p$ with p an integer. A similar density $\bar{\rho}_G$ is defined as an average over all slip systems consistent with the net Burgers vector (see Appendix A). This new variable is termed *effective GND density*.

The distribution of local signed density (i.e. the $|\rho_{+n}^{(\kappa)} - \rho_{-n}^{(\kappa)}|$ terms in (12)) depends on the resolution h with the fluctuations increasing with decreasing h as illustrated in Fig. 12a. Fig. 14 shows the extent to which the effective GND density $\bar{\rho}_G$ is itself depending on resolution. For a given specimen size, the latter is varied from 1 nm to the full height H of the specimen. At any given resolution, and in most cases, three data points are shown which correspond to the three strain levels $\varepsilon = 0.033, 0.067$ and 0.1 . At fixed specimen size and strain level, decreasing h leads to an increase in $\bar{\rho}_G$. This increase is the integral measure of microscopic GND density build-up. At the limit $h = H$, which sets the coarsest resolution, the effective GND density coincides with the actual GND density in the specimen at the current strain ($\bar{\rho}_G = \rho_G$). At the lower limit $h = 1$ nm, the

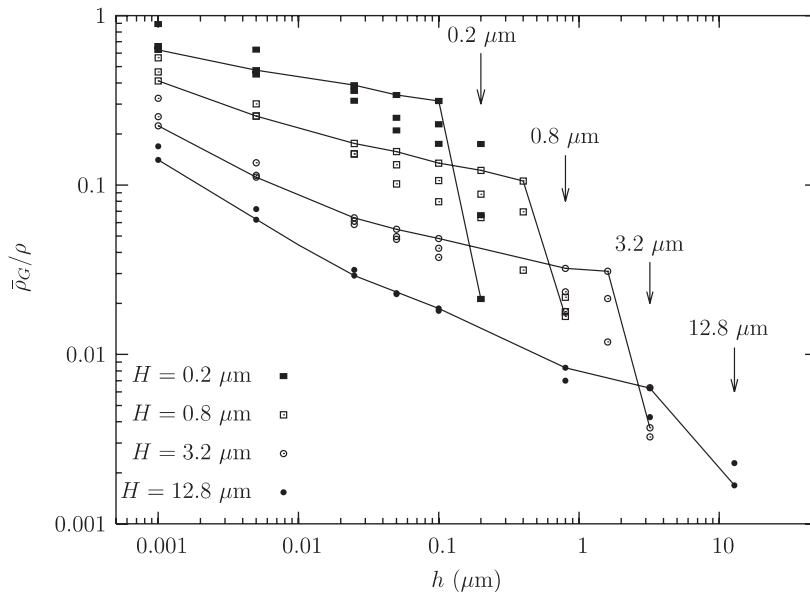


Fig. 14. Effective GND density, $\bar{\rho}_G$, normalized by the total dislocation density versus resolution h for the $H = 0.2, 0.8$ and $3.2 \mu\text{m}$ specimens at three strain levels, $\varepsilon = 0.033, 0.067$ and 0.1 , and for the $H = 12.8 \mu\text{m}$ specimen at $\varepsilon = 0.033$ and 0.056 . Solid lines run through the points corresponding to either $\varepsilon = 0.1$ or 0.056 . The value of $\bar{\rho}_G$ at resolution $h = H$ is identified with the actual GND density ρ_G in the specimen. The densities ρ_G and $\bar{\rho}_G$ are calculated using (A.5) and (A.6), respectively.

dislocation spacing is nearly resolved so that $\bar{\rho}_G$ approaches the total density. In addition, at fixed resolution larger than 25 nm and different from the specimen size, the effective GND density is found to increase with increasing strain with the rate of increase being greater in smaller specimens.

Although definition (12) is resolution-dependent Fig. 14 shows that there is a resolution range over which the sensitivity of the effective GND density to resolution is small in comparison with its sensitivity to specimen size. Roughly speaking the upper and lower limits of that range are 100 and 25 nm.

Next, write the total density as $\rho = \bar{\rho}_G + (\rho - \bar{\rho}_G)$. Several correlations were investigated assuming a two-variable state law for the macroscopic flow stress $\mathcal{F}(\rho, \bar{\rho}_G)$. Because the overall flow stress is the same for either slip system, data corresponding to both slip systems was used to qualify the correlation with more data points. The following additive form has proven most effective based on fits to numerical results (Fig. 15):

$$\mathcal{F} = \mathcal{F}^{(\kappa)} = A\mu b\sqrt{\rho^{(\kappa)} - \bar{\rho}_G^{(\kappa)}} + \mu l^2 \bar{\rho}_G^{(\kappa)}, \quad (13)$$

where A and l are fitting constants. The proposed form is well-defined since $\bar{\rho}_G^{(\kappa)}$ cannot exceed the total density on slip-system κ as shown in Appendix A. The first term of (13) represents a variant of the classical size-independent forest hardening term whereas the second term represents the increase in flow stress associated with the effective GND density. The factor l has dimensions of a length but does not necessarily represent the length scale of the deformation process itself. The results in Fig. 14 clearly indicate that $\bar{\rho}_G$ (or $\bar{\rho}_G^{(\kappa)}$) would essentially vanish in a bulk sample so long as the dislocation spacing is not fully resolved. The scaling law (13) reduces then to the classical Taylor hardening equation (11).

In order to qualify the proposed correlation (13) the data corresponding to the $H = 0.2, 0.8, 3.2$ and $12.8 \mu\text{m}$ specimens within the 25–100 nm resolution range is gathered in Fig. 15. The data correspond to all strain levels shown in Fig. 14. Then viewing \mathcal{F} as a function of $\rho^{(\kappa)}$ and $\bar{\rho}_G^{(\kappa)}$ the factors A and l were determined by linear regression, constraining A to lie between 0.3 and 0.5. The remarkable result is that, even though the effective GND density very much depends on resolution, the length parameter l in (13) was found to be independent of resolution. The fit in Fig. 15 was obtained using $A = 0.3$ and $l = 5.1 \pm 2 \text{ nm}$. Eventually, if densities ρ and $\bar{\rho}_G$ are used in (13) the length l would be $4.0 \pm 2.3 \text{ nm}$.

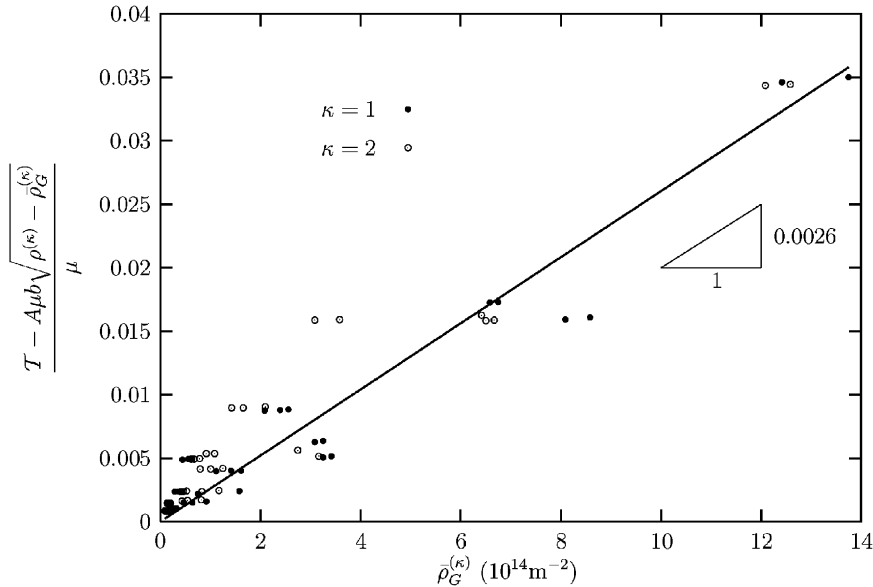


Fig. 15. Qualification of correlation (13) scaling the macroscopic flow stress \mathcal{F} with two state variables: the dislocation density $\rho^{(\kappa)}$ and the effective GND density $\bar{\rho}_G^{(\kappa)}$, specified per slip-system κ to maximize the number of data points. $\bar{\rho}_G^{(\kappa)}$ is defined through (12). The data analyzed include the $H = 0.2$ (two realizations), 0.8 and $3.2 \mu\text{m}$ specimens at three strain levels, $\varepsilon = 0.033, 0.067$ and 0.1 , and the $H = 12.8 \mu\text{m}$ specimen at $\varepsilon = 0.033$ and 0.056 . For each condition three values of the resolution h were used $h = 25, 50$ and 100 nm . There are a total of 84 points in the plot with some overlap. The length scale l in (13) is found to be $5.1 \pm 2 \text{ nm}$ with $A = 0.3$.

3.8. Slip patterns

Fig. 16 shows the distribution of slip at $\varepsilon = 0.1$ in the same specimens shown in Figs. 7 and 9. The computation of total slip γ_{tot} is explained in Appendix B. For all specimen sizes fine slip bands are generated along the whole gauge length of the specimen, in contrast with the slip patterns obtained by Benzerga (2007) in the low dislocation density case where the behavior was essentially multiplication controlled. In sub-micron specimens, the calculations there exhibited single or a few intense slip bands extending across the specimen thickness. Here, the slip bands do not extend across the thickness because slip is restricted by dislocation interactions. The initial dislocation source density is high enough to promote forest hardening mechanisms even in the smallest specimens.

In addition, the slip patterns in Fig. 16 show that in larger specimens slip is more diffuse: the imposed strain rate is accommodated by many more slip bands per unit volume, but the slip bands are more intense in smaller specimens. Also, in regions with high dislocation densities the slip bands are consistently shorter: the dislocations remain the most effective obstacles to the motion of other dislocations in a single crystal.

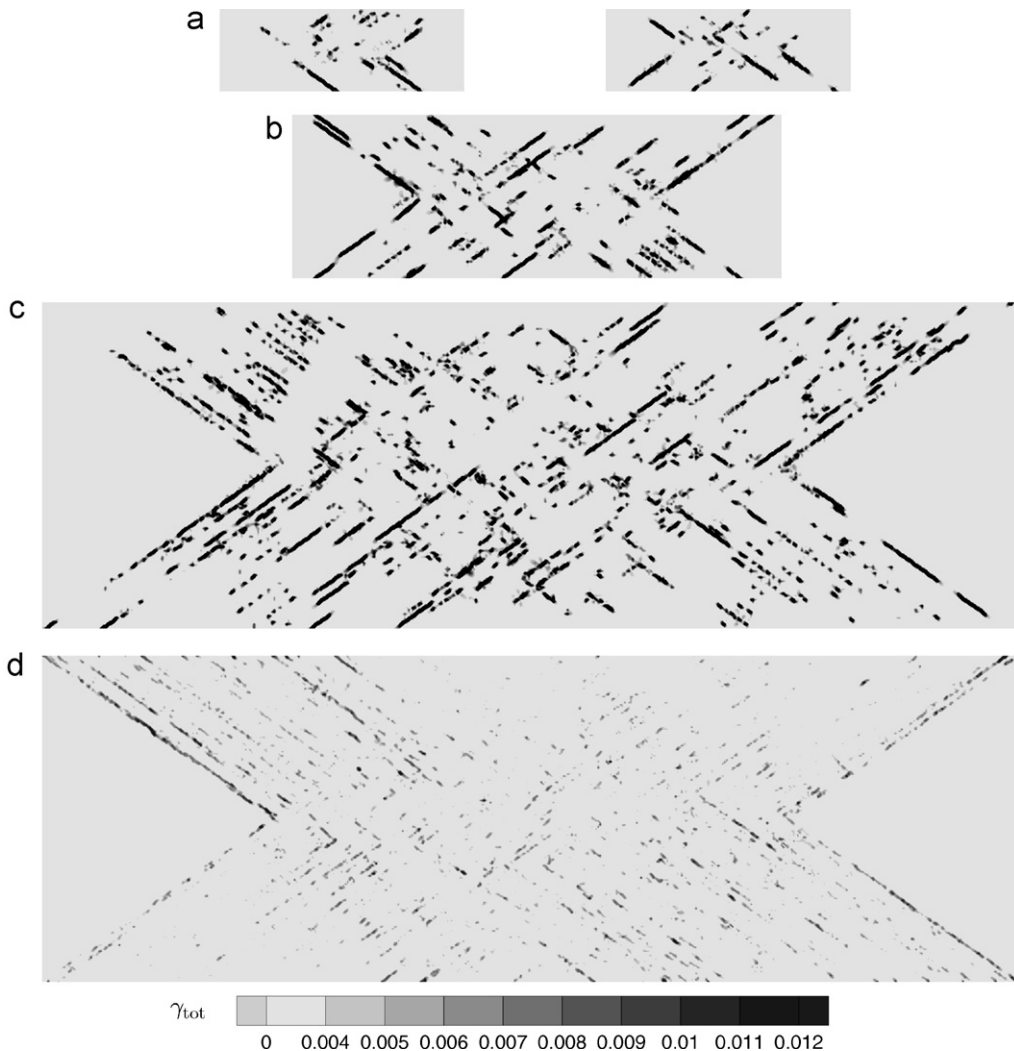


Fig. 16. Contours of total slip γ_{tot} at $\varepsilon = 0.1$ in crystals of height (a) $H = 0.2 \mu\text{m}$; (b) $H = 0.4 \mu\text{m}$; (c) $H = 0.8 \mu\text{m}$ (all scaled appropriately); and (d) $H = 3.2 \mu\text{m}$ (not scaled). Units are arbitrary. Two realizations are shown for the $H = 0.2 \mu\text{m}$ specimen as in Figs. 7 and 9.

4. Discussion

Mechanism-based discrete dislocation plasticity (M-DDP) has been used to analyze the effect of dimensional constraints on plastic flow in the absence of macroscopic strain gradients. A unique capability of the framework is that it permits analyses of the multistage hardening response of single crystals to be undertaken. In particular, the effect of size on work-hardening has been analyzed in detail. The results indicate that the work-hardening rate increases with decreasing specimen size. Our findings demonstrate that this strengthening is due to an increase in stress throughout the specimen when the specimen size is reduced. This increase in stress is associated with the emergence of a signed dislocation density at sufficient resolution. Evidently, the local GND, or signed, density is resolution dependent, but it is worth emphasizing that domains where the GND density does not vanish can be large enough to contain many dislocations and so can be viewed as statistically homogeneous with respect to plastic behavior.

Consistent with a macroscopically homogeneous deformation, no net GND density accumulates over the specimens in general. However, a non-vanishing local GND density emerges in the course of deformation as a result of an evolving dislocation structure. As described by Benzerga et al. (2004), specific dislocation patterns form locally which involve dislocation wall formation, cell closure and cell subdivision. The process of cell closure for instance evolves through the formation of tilt walls that induce lattice misorientations across them. Arrays of GNDs are formed subsequently to accommodate local lattice rotations. Such arrays were referred to as geometrically necessary boundaries (GNBs) by Benzerga et al. (2004). The fact that dislocation structures typical of single and polycrystal deformation involve the formation of GNBs is well appreciated in the literature (Hughes and Hansen, 1993). Although the patterns described above are planar, they do have in common with those described by Hughes and Hansen (1993) that they lead to significant lattice rotations and build-up of *local* GND density.

An important aspect of the behavior predicted by the M-DDP calculations here is that Taylor-like hardening breaks down at the macro-scale, i.e. that of the sample. The scaling law (11) characteristic of bulk behavior ceases to be valid even in the largest specimens analyzed after sufficient straining. In addition, the deviation from (11) is found to increase in magnitude and to occur at a lower strain with decreasing specimen size (Fig. 8). Previous discrete dislocation analyses carried out by Benzerga et al. (2004) within the same framework did not explore size effects. The values of $\Theta_{II}/\mu = 0.022$ and 0.025 predicted in their analyses for specimens with $H = 2$ and $4\mu\text{m}$, respectively, are about three times the average bulk value and fall slightly below the curve in Fig. 4b. This difference is attributed to the lower strain rate of order 100 s^{-1} used by Benzerga et al. (2004). Also their analyses indicated that Eq. (11) was valid over the full strain range they investigated. One key difference between their analyses and those reported here is the strain level and dislocation density reached in the simulations. Here, the calculations were conducted up to a strain of 0.1 whereas those that exhibited comparable hardening rate in (Benzerga et al., 2004) were limited to strains of 0.05; also, the dislocation densities reached in the present simulations are up to one order of magnitude higher.

Most importantly, the present M-DDP calculations demonstrate that Taylor-like hardening breaks down at the micro-scale, i.e. that of a non-vanishing GND density. This is best illustrated by the results selected in Fig. 11b. This finding raises fundamental questions regarding the formulation of augmented theories of plasticity. Many such theories are based on the understanding that plastic flow processes are inherently size-independent in the absence of strain gradients at the scale of the elementary volume. For instance, some theories presume as valid the scaling of the flow stress with the dislocation density at the micro-scale (Nix and Gao, 1998; Gao et al., 1999). Although the M-DDP analyses predict that the scaling law (11) breaks down under conditions of macroscopically homogeneous deformation, it is likely that (11) will break down under macroscopically inhomogeneous deformation as well.

The scale dependence of strength and hardening beyond yielding and in the absence of macroscopic strain gradients poses a challenge to modeling of plasticity at the micron scale. Non-local plasticity theories, in their current form, fail to capture size effects under nominally uniform deformation. In general, the length scales that enter such theories stem from dimensional considerations and thus are not tied to the physics of deformation. In addition, the length scales of non-local plasticity theories are fixed whereas plastic deformation involves evolving length scales. A coarse-grained version of so-called field-dislocation mechanics

(Acharya, 2001, 2004; Roy and Acharya, 2006) begins to show the promise of predicting size-dependency in the absence of macroscopic gradients.

It remains that the size effect predicted by the calculations here is directly linked to GNDs. From that point of view, it is no different in essence from the plasticity size effect documented for nanoindentation of films or bending of foils. The scale at which GNDs operate is smaller, however, under macroscopically homogeneous deformation. As a consequence, the scale dependence of plastic flow arises in a specimen size range below $10\ \mu\text{m}$ or so. On the other hand, under inhomogeneous deformation this scale dependence is already noticeable for a specimen size about $100\ \mu\text{m}$ (Stölken and Evans, 1998).

From the practical standpoint, because of the size-dependence of strain hardening (Fig. 4b), the power law scaling (10) of the flow stress changes upon deformation. Our calculations predict a scaling exponent in the range 0–0.42 for strains ranging from yield to 0.1 (Figs. 2 and 4a). The discrete dislocation calculations of Benzerga and Shaver (2006) and similar recent unpublished work predict a value of x larger than unity whereas those carried out by Deshpande et al. (2005) predict $x = 0.5$, closer to the value predicted here at $\varepsilon = 0.1$. The main difference between the two sets of calculations is directly related to the density of initial dislocation sources. At low initial densities (typically $1\ \mu\text{m}^{-2}$ and below) the behavior is multiplication controlled as in Benzerga and Shaver (2006). On the other hand, at high initial dislocation density (typically $100\ \mu\text{m}^{-2}$ and above) the behavior is rather dislocation-interaction controlled. The two sets of studies are thus complementary of each other in that they explore two extreme scenarios, which help shed some light on the micro-pillar experimental results. Experimental reports of the flow stress scaling indicate values of the scaling exponent x ranging from 0.6 in Au microcrystals at $\varepsilon = 0.05$ (Volkert and Lilleodden, 2006) to 0.6–0.7 in Ni microcrystals at $\varepsilon = 0.01$ (for diameters larger than $1\ \mu\text{m}$) (Dimiduk et al., 2005) to a value as high as $x = 1.1$ at $\varepsilon = 0.1$ in gold microcrystals with diameters in the sub-micron range (Greer and Nix, 2006). Note that these experimental values are often determined after some plastic straining; hence they are not representative of the scaling of the flow stress over the full strain range. Yet the 0.6–1.1 range of experimental values is contained within the 0.4–1.5 range of predicted values, and this suggests that the behavior observed in micropillars may be affected by multiplication as well as interaction processes but in proportions that may vary with density and strain level.

In light of the recent micropillar experiments along with discrete dislocation predictions like those presented here, it would be a subtle task to apportion the origin of size effects in previous experiments where strain gradients were superposed onto a homogeneous component of the applied strain. In particular, the enhanced size effect reported in recent studies (Swadener et al., 2002) for nanoindentation at the sub-micron scale may be the signature of the emergence of strain gradients and related GND densities at a scale much smaller than that associated with the gradient part of the imposed strain.

In our view, it is worthless to pursue a universal correlation between flow stress and dislocation density that would be valid at all scales. One should be content if a scaling law can be at all inferred and accept that the involved constants may be resolution-dependent. The results of the present M-DDP analyses have been used to derive and qualify a correlation between the *macroscopic* flow stress, the dislocation density and an appropriate *macroscopic* measure of the microscopic GND density. One remarkable aspect of the flow stress scaling relation (13) is that, while the effective GND density depends on resolution, factors A and l do not. Thus, the proposed correlation can be used as a fundamental law in physics-based phenomenological modeling of plastic behavior at the micron scale.

The additive form in the generalized Taylor equation (13) was motivated in part by the fact that there is a strong connection between the emergence of a local GND structure and the Bauschinger effect. At low strains the local GND density is very small relative to the total density. As a consequence the classical scaling law (11) holds (Fig. 8) and the Bauschinger effect is small (Fig. 13). By way of contrast, at higher strains typical of stage II the local GND density is significant and so is the Bauschinger effect. Such a strong effect indicates that a significant portion of the flow stress results from back-stresses. The effect of the latter is inherently different from that associated with forest hardening. It is therefore not surprising that a linear, rather than square root, dependence upon the effective GND density was found to fit better the M-DDP results.

Ultimately, there is no substitute to injecting appropriate physics in developing a better understanding of size-dependent plasticity. Despite the idealization inherent to the representation of dislocation reactions within M-DDP, the merit of the framework is to enhance the capability of mesoscale modeling at capturing the

richness of collective dislocation behavior without too much compromise to computational power. Most calculations carried out here were run on a Linux desktop. Only those calculations corresponding to the largest three specimens were carried out on a supercomputer using a sequential code. Ongoing efforts at parallelizing the code and improving dislocation dynamics algorithms will impart further capabilities to the framework.

5. Conclusions

Discrete dislocation analyses of the uniaxial compression of single crystals potentially oriented for double slip have been carried out to investigate the effect of specimen size on plastic flow properties. The calculations are two-dimensional but key physics of the three-dimensional dislocation interactions were incorporated through additional constitutive rules. Such “2.5D” rules account for line tension, junction formation and destruction, and dynamic source and obstacle creation. Within this framework, plastic flow arises from the nucleation and subsequent motion of discrete dislocations. The multi-stage hardening response as well as the evolving dislocation structure are natural outcomes of the simulations. In this work, a relatively high density of pre-existing internal Frank–Read sources was used to promote athermal hardening processes. Our conclusions are as follows:

- Strengthening upon scale reduction is predicted under nominally uniform compression. The size effect is significant for both the flow stress and the work-hardening rate. In particular, the stage II hardening rate increases by one order of magnitude within the range of specimen sizes explored here.
- The rate of dislocation accumulation increases with decreasing specimen size. However, the flow stress is not set by the dislocation density as in bulk plasticity; Taylor-like hardening breaks down at both macro- and micro-scales.
- Although in general no net GND density accumulates in the specimens, consistent with a macroscopically homogeneous deformation, a microscopic GND density emerges in the course of deformation, which strongly affects the microscopic, hence the macroscopic, flow stress.
- The emergence of a local GND density results from microstructure evolution and is associated with a strong Bauschinger effect. The evolution of the dislocation structure is promoted by increased dislocation interactions fostered by the usual athermal hardening processes, but with characteristic lengths comparable with the size of submicron-scale specimens. The size effect results.
- A new scaling law for the flow stress is proposed based on the discrete dislocation analyses. Two state variables are used: the dislocation density and an effective GND density. The latter depends on resolution but the scaling parameters do not.
- The size effect predicted here stems from interaction controlled behavior, which primarily affects the hardening and is promoted at high dislocation density. On the other hand, at low dislocation densities forest hardening mechanisms are less effective and the behavior may become multiplication controlled. Both types of behavior may be invoked in interpreting the results of recent micropillar experiments.

Acknowledgments

The authors acknowledge a grant from the Texas A&M University Supercomputing Facility.

Appendix A. Calculation of the actual and effective GND densities

Consider a volume ω of crystalline material that is plastically deformed by slip on N_s slip systems. Assuming plane strain, the density of geometrically necessary dislocations over ω is defined as the Euclidean norm of the net Burgers vector, to be specified below, per unit material Burgers vector length, i.e.

$$\rho_G = \frac{\|\mathbf{B}\|}{b} = \frac{\sqrt{B_i B_i}}{b}. \quad (\text{A.1})$$

Following the formulation in [Cermelli and Gurtin \(2001\)](#) a network of dislocations piercing a plane with unit normal \mathbf{n} has a net Burgers vector \mathbf{B} per unit area given by

$$\mathbf{B} = \mathbf{Gn}, \tag{A.2}$$

where \mathbf{G} is the geometric dislocation tensor. Assuming infinitesimal rotations, and to the neglect of elastic strains, \mathbf{G} reduces to Nye’s tensor $\boldsymbol{\alpha}$ ([Nye, 1953](#)).

For pure edge dislocations under the assumed plane strain conditions \mathbf{n} is chosen as the out of plane normal $\mathbf{e}_1 \times \mathbf{e}_2$ with \mathbf{e}_1 and \mathbf{e}_2 the base vectors in the x_1 – x_2 plane of [Fig. 1](#). The components of Nye’s tensor on that base are written as ([Arsenlis et al., 2004](#))

$$\alpha_{ij} = \sum_{\kappa=1}^{N_s} (\rho_+^{(\kappa)} - \rho_-^{(\kappa)}) b_i^{(\kappa)} n_j, \tag{A.3}$$

where $\mathbf{b}^{(\kappa)}$ is the Burgers vector of slip-system κ and is here written as $b\mathbf{s}^{(\kappa)}$ with $\mathbf{s}^{(\kappa)}$ a unit vector along the slip direction. Thus, under the conditions of the simulations here, Eq. (A.2) is specified in view of (A.3) as

$$B_i = b \sum_{\kappa=1}^{N_s} (\rho_+^{(\kappa)} - \rho_-^{(\kappa)}) s_i^{(\kappa)}. \tag{A.4}$$

Denoting $\varphi^{(\kappa)}$ the oriented angle that defines slip direction on slip-system κ , measured from the x_1 -axis, the formula used to calculate ρ_G is then obtained as

$$\rho_G = \sqrt{\left[\sum_{\kappa} (\rho_+^{(\kappa)} - \rho_-^{(\kappa)}) \cos \varphi^{(\kappa)} \right]^2 + \left[\sum_{\kappa} (\rho_+^{(\kappa)} - \rho_-^{(\kappa)}) \sin \varphi^{(\kappa)} \right]^2}. \tag{A.5}$$

For the double slip configuration considered here, $\varphi^{(1)} = \varphi_0 = 35.25^\circ$ and $\varphi^{(2)} = \pi - \varphi_0 = 144.75^\circ$.

The effective GND density $\bar{\rho}_G$ is defined as

$$\bar{\rho}_G = \sum_{n=1}^p \frac{\Omega^n}{\Omega} \rho_{Gn}, \tag{A.6}$$

where ρ_{Gn} is the GND density calculated as in (A.5) but specified over the local domain Ω^n defined in the text.

Since a correlation of the form (13) is sought, the positiveness of $\rho^{(\kappa)} - \bar{\rho}_G^{(\kappa)}$, specified for each slip system, is in question. The inequality $\rho^{(\kappa)} \geq \bar{\rho}_G^{(\kappa)}$, with $\bar{\rho}_G^{(\kappa)}$ given by (12), follows from the identity:

$$\rho_n^{(\kappa)} = |\rho_{+n}^{(\kappa)} - \rho_{-n}^{(\kappa)}| + 2 \min(\rho_{+n}^{(\kappa)}, \rho_{-n}^{(\kappa)}), \tag{A.7}$$

which is valid for each domain Ω^n . If a correlation where $\rho - \bar{\rho}_G$ is used instead, the inequality $\rho \geq \bar{\rho}_G$, with $\bar{\rho}_G$ given by (A.6), holds true because the actual GND density within a given domain cannot exceed the total density in that domain.

Appendix B. Determination of slip contours

Since in discrete dislocation plasticity, the plastic part of the deformation is associated with the evolution of displacement jumps across the slip planes, the displacement gradient field involves delta functions which need to be accounted for to compute the slip. To simplify the calculation, an approximation is used. A smooth strain rate field, $\dot{\boldsymbol{\epsilon}}^s$, is introduced in each finite element that is computed by differentiating the total displacement rate field $\dot{\mathbf{u}}$ in that element using the finite element shape functions. Then, within an element, the slip on the κ -th system is defined by

$$\gamma^{(\kappa)} = s_p^{(\kappa)} \dot{\epsilon}_{pq}^s m_q^{(\kappa)}, \tag{B.1}$$

where $\mathbf{s}^{(\kappa)}$ is the slip direction and $\mathbf{m}^{(\kappa)}$ the slip normal for slip-system κ . Because $\gamma^{(\kappa)}$ includes contributions from all dislocations it does not represent the actual slip on system κ . It is rather viewed as a convenient measure for visualizing the slip patterns. The pointwise total slip is defined as $\gamma_{\text{tot}} = \sum_{\kappa=1,2} |\gamma^{(\kappa)}|$. Note that slip

displacements associated with dislocations exiting at free surfaces are accounted for in (B.1) although no account is taken of actual geometry changes, e.g. creation of new free surface.

References

- Acharya, A., 2001. A model of crystal plasticity based on the theory of continuously distributed dislocations. *J. Mech. Phys. Solids* 49, 761–784.
- Acharya, A., 2004. Constitutive analysis of finite deformation field dislocation mechanics. *J. Mech. Phys. Solids* 52, 301–316.
- Arsenlis, A., Parks, D.M., Becker, R., Bulatov, V.V., 2004. On the evolution of crystallographic dislocation density in non-homogeneously deforming crystals. *J. Mech. Phys. Solids* 52, 1213–1246.
- Benzerga, A. A., 2007. An analysis of exhaustion hardening in micron-scale plasticity, submitted for publication.
- Benzerga, A.A., Shaver, N.F., 2006. Scale dependence of mechanical properties of single crystals under uniform deformation. *Scr. Mater.* 54, 1937–1941.
- Benzerga, A.A., Bréchet, Y., Needleman, A., Van der Giessen, E., 2004. Incorporating three-dimensional mechanisms into two-dimensional dislocation dynamics. *Modelling Simul. Mater. Sci. Eng.* 12, 159–196.
- Benzerga, A.A., Bréchet, Y., Needleman, A., Van der Giessen, E., 2005. The stored energy of cold work: predictions from discrete dislocation plasticity. *Acta Mater.* 53, 4765–4779.
- Cermelli, P., Gurtin, M.E., 2001. On the characterization of geometrically necessary dislocations in finite plasticity. *J. Mech. Phys. Solids* 49, 1539–1568.
- Deshpande, V.S., Needleman, A., Van der Giessen, E., 2005. Plasticity size effects in tension and compression of single crystals. *J. Mech. Phys. Solids* 53, 2661–2691.
- Dimiduk, D.M., Uchic, M.D., Parthasarathy, T.A., 2005. Size-affected single-slip behavior of pure nickel microcrystals. *Acta Mater.* 53, 4065–4077.
- Espinosa, H.D., Panico, M., Berbenni, S., Schwarz, K.W., 2006. Discrete dislocation dynamics simulations to interpret plasticity size and surface effects in freestanding fcc thin films. *Int. J. Plasticity* 22, 2091–2117.
- Fleck, N.A., Hutchinson, J.W., 2001. A reformulation of strain gradient plasticity. *J. Mech. Phys. Solids* 49, 2245–2271.
- Fleck, N.A., Muller, G.M., Ashby, M.F., Hutchinson, J.W., 1994. Strain gradient plasticity—theory and experiment. *Acta Metall. Mater.* 42, 475–487.
- Forest, S., Sievert, R., 2003. Elastoviscoplastic constitutive frameworks for generalized continua. *Acta Mech.* 160, 71–111.
- Fourie, J.T., 1968. The flow stress gradient between the surface and centre of deformed copper single crystals. *Philos. Mag.* 17, 735–756.
- Gao, H., Huang, Y., Nix, W.D., Hutchinson, J.W., 1999. Mechanism-based strain gradient plasticity—I. Theory. *J. Mech. Phys. Solids* 47, 1239–1263.
- Gil Sevillano, J., 1993. Flow stress and work hardening. In: Cahn, R.W., Haasen, P., Kramer, E., Mughrabi, H. (Eds.), *Materials Science and Technology*. vol. 6. VCH, Weinheim, pp. 19–88.
- Greer, J.R., Nix, W.D., 2006. Nanoscale gold pillars strengthened through dislocation starvation. *Phys. Rev. B* 73, 245410.
- Greer, J.R., Oliver, W.C., Nix, W.D., 2005. Size dependence of mechanical properties of gold at the micron scale in the absence of strain gradients. *Acta Mater.* 53, 1821–1830.
- Gurtin, M.E., 2002. A gradient theory of single-crystal viscoplasticity that accounts for the geometrically necessary dislocations. *J. Mech. Phys. Solids* 50, 5–32.
- Hughes, D.A., Hansen, N., 1993. Microstructural evolution in nickel during rolling from intermediate to large strains. *Met. Trans. A* 24, 2021–2037.
- Nix, W.D., Gao, H., 1998. Indentation size effects in crystalline materials: a law for strain gradient plasticity. *J. Mech. Phys. Solids* 46, 411–425.
- Nye, J.F., 1953. Some geometrical relations in dislocated crystals. *Acta Metall.* 1, 153–162.
- Roy, A., Acharya, A., 2006. Size effects and idealized dislocation microstructure at small scales: predictions of a phenomenological model of mesoscopic field dislocation mechanics: part ii. *J. Mech. Phys. Solids* 54, 1711–1743.
- Stölken, J.S., Evans, A.G., 1998. A microbend test method for measuring the plasticity length scale. *Acta Mater.* 46, 5109–5115.
- Swadener, J.G., George, E.P., Pharr, G.M., 2002. The correlation of the indentation size effect measured with indenters of various shapes. *J. Mech. Phys. Solids* 50, 681–694.
- Uchic, M.D., Dimiduk, D.M., Florando, J.N., Nix, W.D., 2004. Sample dimensions influence strength and crystal plasticity. *Science* 305, 986–989.
- Van der Giessen, E., Needleman, A., 1995. Discrete dislocation plasticity: a simple planar model. *Modelling Simul. Mater. Sci. Eng.* 3, 689–735.
- Volkert, C.A., Lilleodden, E.T., 2006. Size effects in the deformation of sub-micron Au columns. *Philos. Mag.* 86, 5567–5579.
- von Blanckenhagen, B., Gumbsch, P., Arzt, E., 2001. Dislocation sources in discrete dislocation simulations of thin-film plasticity and the Hall-Petch relation. *Modelling Simul. Mater. Sci. Eng.* 9, 157–169.